Microstructure-sensitive Crystal Viscoplasticity for Ni-base Superalloys Targeting Long-term Creep-Fatigue Interaction Modeling

Year 4 Report

Reporting Period: October 1, 2016 to September 30, 2017

Professor Richard W. Neu

Graduate Research Assistants:
Ernesto Estrada Rodas, Sanam Gorgan Nejad, Anirudh Bhat

George W. Woodruff School of Mechanical Engineering /
School of Materials Science and Engineering
Georgia Institute of Technology
Atlanta, GA 30332

September 30, 2017

U. S. Department of Energy
National Energy Technology Laboratory
University Turbine Systems Research
Award: DE-FE0011722

Topic Area 2 – Hot Gas Path Research and Development

DISCLAIMER

ABSTRACT

The aim of this project is to develop a microstructure-sensitive crystal viscoplasticity (CVP) model for single-crystal Ni-base superalloys to model the behavior of the material and components in the hot gas path sections of industrial gas turbines (IGT). Microstructure degradation associated with aging critical to predicting long-term creep-fatigue interactions will be embedded into the model through the γ' precipitate morphology evolution by coupling the coarsening drivers and kinetics into the constitutive equations of the CVP model. Model parameters will be determined using new experimental protocols that involve systematically artificially aging the alloy under different stress conditions to determine the relationship between the size and morphology γ' precipitates on the creep and thermomechanical fatigue response.

TABLE OF CONTENTS

EXECUTIVE SUMMARY

With increasing hot gas path temperature, more demands are placed on the materials in the hot gas path, requiring designs to employ single crystal Ni-base superalloys in industrial gas turbines (IGT). Completely eliminating grain boundaries improves creep behavior but increase temperatures also increases thermal transients. Currently, "short" duration (<3000 cycles (TMF), <30,000 hrs (Creep)) laboratory tests are used to predict component lifetimes designed to be greater than these cycles and times. A critical limitation of current remaining life prediction models is that they do not explicitly account for the changes in the microstructural degradation occurring under high temperature exposure over long-term service conditions typical of IGT. Therefore, consideration of microstructural degradation is key to developing more robust creep-fatigue life models for these hot section alloys to extend predictions outside the typical laboratory test regime. Another critical limitation of current remaining life prediction models is that they do not explicitly account for the duty cycle such as peakers or baseload operation of IGT and understanding the microstructural changes during usage will also be key to predict the residual life of the components.

The understanding of the effects of aged microstructures on the thermomechanical properties of Ni-base superalloys remains unclear. Of the few experimental results available in this area, the results are mixed, some promote aged microstructures as beneficial, while others as detrimental. The importance of these aged structures arises from the fact that when components used in the hot sections of IGT engines remain in service for extended periods of time, the local temperature and stress provides the catalyst for the evolution of the microstructure. Further, in the design of components that comprise the hot sections of IGTs, designers use material models assuming the mechanical properties are that of the as-cast and heat-treated material even for simulations of years of the component usage.

To account for these extreme hot section environments employing highly anisotropic single-crystal alloys, a physics-based temperature-dependent, microstructure-sensitive life analysis tool based on crystal viscoplasticity (CVP) is being developed that captures

i. the crystal orientation which controls both elastic and inelastic anisotropy,
ii. the temperature dependence on the mechanism of the creep deformation and its interaction with microstructure and low-temperature fatigue deformation mechanism,
iii. complex cyclic thermomechanical boundary conditions leading to extreme local thermal gradients,
iv. the influence of the evolution of microstructure (e.g., coarsening and rafting of the γ') with long-term exposure to elevated temperature under sustained stress through internal state variables without explicitly modeling the γ' precipitates and γ matrix, and
v. the influence of the evolution of microstructure near exposed surfaces due to environmental considerations such as oxidation and embrittlement.

Constitutive models available in commercial finite element codes used to address creep-fatigue interactions in single crystal Ni-base superalloys are limited to non-interaction creep and plasticity models which cannot address the physical processes or microstructural evolution. An enhanced CVP model is needed that has broad utility in the design and maintenance of hot section materials

and components of IGT when conventional isotropic creep-fatigue constitutive models are not applicable. The CVP enables the engineer to predict component response using thermomechanical boundary conditions, to understand the influence of thermal transients associated with efficient and effective cooling strategies as well as load-cycle gas turbines, to perform component analysis investigating the interaction between geometric discontinuities and crystal orientation of the material, to determine the crack tip stress fields for predicting creep-fatigue crack growth, and to study role of defects such as freckles important for process and materials design.

This report summarizes work performed in Year 4 including aging studies conducted on single crystal Ni-base superalloy CMSX-8, and the development of the microstructure-sensitive CVP model for CMSX-8 including its calibration from creep-fatigue experiments and its implementation in analysis codes. The details of this work are described in two documents recently prepared: "Creep-Fatigue Interactions in the Single-Crystal Ni-base Superalloy CMSX-8" (Appendix 1) and "Crystal Viscoplasticity Model for the Creep-Fatigue Interactions in the Single-Crystal Ni-base Superalloy CMSX-8" (Appendix 2).

APPENDIX 1

Creep-Fatigue Interactions in the Single-Crystal Ni-base Superalloy CMSX-8

S. Gorgannejad [a], Ernesto A. Estrada Rodas [a], R.W. Neu [a,b]

[a] *Georgia Institute of Technology, George W. Woodruff School of Mechanical Engineering, Atlanta, GA*

[c] *Georgia Institute of Technology, School of Materials Science and Engineering, Atlanta, GA*

Abstract

The creep-fatigue interaction of the CMSX-8 single-crystal Ni-base superalloy has been studied by introducing a sequential experimental workflow that examines the influence of creep in altering the isothermal low-cycle fatigue response and vice versa. The adopted prior-treatment followed by fatigue loading was aimed to decouple and investigate the effect of γ/γ' morphological evolution and accumulated inelastic strain associated with creep deformation separately on fatigue properties at 20 ^{o} C, 750 ^{o} C, and 1100^{o} C. The results showed the extent of deleterious impact strongly relies on the fatigue temperature range and the dominant deformation mechanism. The pre-fatigue treatment with subsequent creep-rupture tests were conducted at 20 ^{o} C and 1100 ^{o} C. Two creep conditions were selected at 800 ^{o} C and 900 ^{o} C in such a way that the primary creep is promoted in the former and absent in the latter one. Similarly, the temperature of the pre-fatigue treatment was found to be critical in deteriorating creep-fatigue life and ductility. The findings are supported by the fractography study on the fatigue samples.

Keywords: creep-fatigue interaction, low-cycle fatigue, creep, fractography, Ni-base superalloy, CMSX-8.

Introduction

The performance of the gas turbine engines used for jet propulsion or electricity generation in land-based turbines is highly dependent on the conditions of the gas at the entry of the turbine arrangement. There is a major focus on the Turbine Entry Temperature (TET) to constantly raise as it enhances the efficiency of the engine by reducing the fuel consumption and cost as well as pollution considerably [1, 2] . Therefore, improving the temperature capability of the materials used in the hot section of the gas turbine is an ongoing demand in materials design [3, 4]. Nickel-based superalloys have widely been the material of choice for high-temperature applications, particularly in gas turbine engine industry owing to the superior resistance they provide under static and cyclic loading at elevated temperatures close to their melting points, substantial stability under creep conditions and long-term exposure to mechanical and environmental degradation [5].

In conjunction with the cyclic loading that turbine blade materials experience at elevated temperatures, depending on the hold time and strain range, they are subjected to time-dependent thermally-induced creep deformation as well. The imposed hold time at maximum load in land-based turbines can reach up to several days [5]. Incorporation of the creep-fatigue interaction study in the characterization of the turbine airfoil materials is critical to obtain realistic insight into the performance of the engines. Researchers have employed various methods and approaches to simulate creep-fatigue interaction (CFI) conditions of an actual operating

component through designing different test protocols [6-10]. Each of the adopted methodologies enlightens one facet of such an interaction and ultimately results in a comprehensive understanding of the phenomenon. An approach commonly taken is to incorporate hold times which induces creep effect to every fatigue cycle [11-13] (Figure 1 (a)). The hold time might be exerted under stress- or strain-controlled modes at the maximum and minimum magnitude of loading profile.

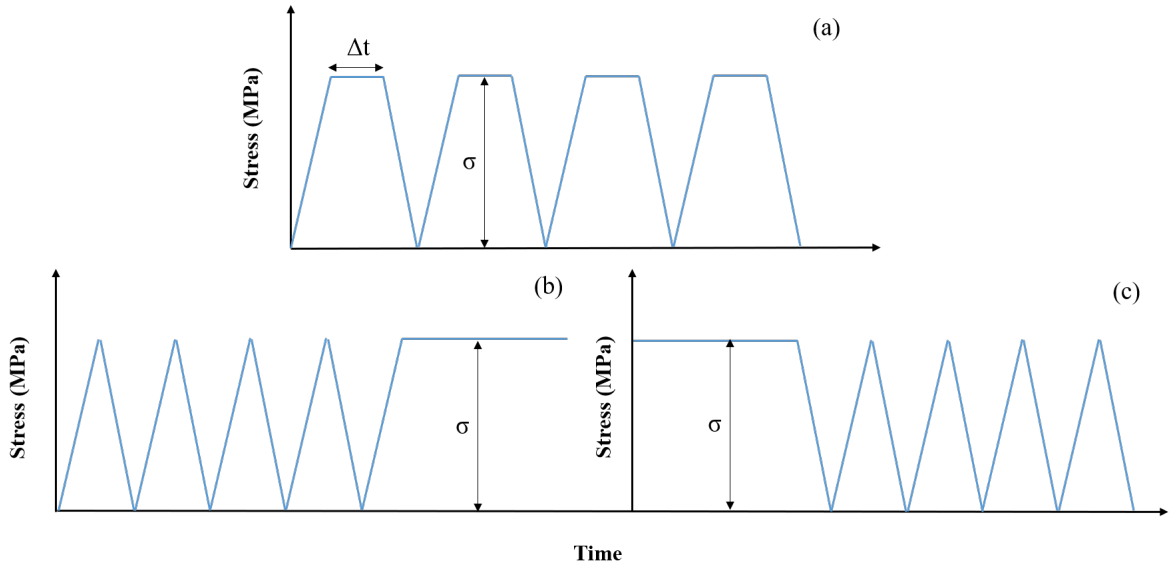

Figure 1 Schematic of stress profile of load-controlled (a) creep-fatigue interaction (b) fatigue followed by creep and (c) creep followed by fatigue testing.

An alternative approach to investigate the creep-fatigue interaction is to adopt sequential experiments by which the effect of fatigue damage on creep response and conversely, creep damage on fatigue life are assessed [6, 9, 14]. In either case, at first, the material experiences fatigue or creep to a predetermined number of cycles or creep strain; and subsequently, the sample is subjected to creep or fatigue loading until the failure point is reached. Studies of Pierce et al. [9] on PWA1484 single-crystal nickel-base superalloy showed that prior fatigue diminishes the subsequent primary creep strain as well as creep strain rate while the secondary creep strain rate remains invariant and independent of the pre-treatment. On the other hand, the influence that prior creep exerts on fatigue life is more complicated and potent. The degradation that the material is subjected to as a result of prior creep is attributed to the microstructural evolution, particularly rafting, porosity growth and TCP phase formation at elevated temperatures. It is suggested that the influence of the microstructure degradation on fatigue life is more pronounced and detrimental than other creep-induced damage mechanisms [14].

Elimination of the grain boundaries of the Ni-base superalloys induces the exceptionally high-temperature tolerance. However, microstructural degradation is imposed on the material during operation that alters the properties and response of the component. Directional coarsening, so-called rafting or directional coarsening, that is formed under the combined influence of stress and high temperature is the most common type of microstructure degradation in Ni-base superalloys [15-17]. It is well understood that the creep and fatigue performance of Ni-base superalloys strongly relies on the morphology of γ/γ' structure. The distinct properties

of this class of materials are ascribed to the FCC γ matrix and the ordered γ′ precipitates with $L1_2$ structure. Coarsening of the initial γ′ precipitates by 25%, leads to nearly 10 times smaller primary creep strain for PWA1484 single-crystal nickel-base superalloy, due to the fact that, it becomes more difficult for the dislocation ribbons to cut through γ′ precipitates as the particle sizes are increasing [9]. In addition, Epishin et al. [18] observed that creep-induced rafting alters the stress-strain diagram of CMSX-4 and reduces the yield strength, particularly at room temperature. At higher temperatures, under uniaxial loading, the deteriorative influence of degraded microstructure manifests itself in decreasing the ultimate yield strength of the material. They also examined the low cycle fatigue (LCF) behavior of CMSX-4 at 700°C on a sample with a fully rafted microstructure that is subjected to creep strain to the end of primary creep and showed that fatigue life decreased to 1/8 after creep in 1150°C [14]. This observation was confirmed by Ott and Mughrabi [19] studies on monocrystalline CMSX-4 and CMSX-6 for high-temperature LCF condition. It was indicated that the sensitivity of fatigue life to the microstructural degradation is stronger once the strain amplitude exceeds the elasticity limit of the virgin CMSX-4 ($\Delta\varepsilon > 0.9\%$) [18].

So far, the role of the microstructure in the exploration of the creep-fatigue interaction of second-generation Ni-base single-crystal superalloys (SX) has not been the focus of much discussions and while many studies have covered the response of the CMSX-4, no study has examined the low Re-content CMSX-8 to the best of our knowledge. The present work aims to employ the sequential type of experiments to evaluate the influence of pre-treatments including prior creep and prior microstructural degradation (rafting and coarsening) on LCF performance of the CMSX-8 single-crystal Ni-base superalloy and compares them against the conventional creep-fatigue interaction (CFI) tests that are associated with hold times. Additionally, the impact of the prior fatigue on the creep curve has been studied to enable a great deal of insight and understanding on the creep-fatigue interaction of the material.

Material

Development of SX alloys in the late 1970's was associated with the introduction of new alloying elements (Re and Ru) that primarily offered enhanced creep-rupture life [4]. The first, second and third generation of single-crystal Ni-base superalloys has been classified according to their Re content. CMSX-4 is the benchmark alloy for second-generation Ni-base superalloys and it contains 3 wt% Re [20]. However, due to the scarcity and limited market, the application of CMSX-4 has found to be not economically reasonable in industrial gas turbines. As a result, Cannon-Muskegon Corporation developed CMSX-8 superalloy with similar composition as CMSX-4, to achieve excellent creep-rupture property, acceptable phase stability, and good oxidation resistance, but with reduced Re content by one half [21]. The nominal composition of CMSX-8 is provided in Table 1.

Table 1 CMSX-8 nominal composition

Element	wt%	Element	wt%
Cr	5.4	Re	1.5
Co	10	Al	5.7
Mo	0.6	Ti	0.7

Ta	8	Hf	0.2
W	8	Ni	Balance

The typical two-phase solution heat-treated microstructure of CMSX-8 is illustrated in Figure 2 (a), in which two strengthening mechanisms are combined; the solid solution hardening at γ channels and precipitation hardening introduced by the high-volume fraction of the coherent $L1_2$-ordered phase. The disordered γ phase with FCC structure exhibits a high concentration of solid solution elements such as cobalt, chromium, and rhenium. Re is a potent element to improve the thermal stability of the Ni-base superalloys and addition of this rare element to the composition delays microstructure degradation by slowing diffusion and eventually enhances the creep resistance [5, 22].

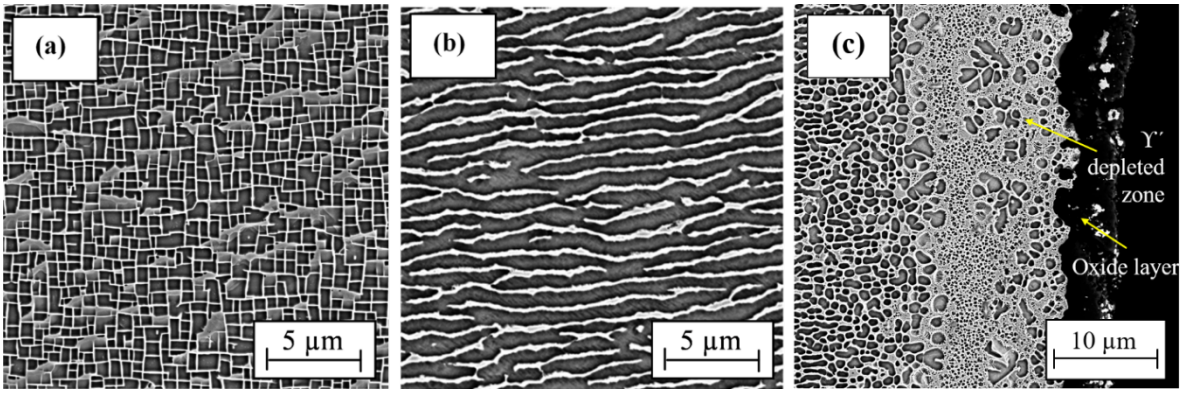

Figure 2 The CMSX-8 microstructure at (a) as-heat-treated (b) fully rafted state. (c) formation of oxide layer and γ′ depleted zone at 1100 ˚C.

The single-crystal bars were casted by Precision Case Component (PCC) airfoils Inc. in <001> direction and solution and double age treated using proprietary conditions that is typical for blade materials to create the desired γ/γ′ microstructure with 0.7 ± 0.03 volume fraction of the cuboidal precipitates and the average size of 0.74 μm. Thereafter, the dogbone specimens with gage diameter and length of 6.35 and 12.7 mm were machined out of the single-crystal bars.

Mechanical Testing

As was mentioned earlier, the time-dependent creep deformation is associated with microstructure evolution. To independently investigate the influence of the microstructural degradation and plastic deformation induced by creep phenomenon on the fatigue behavior, two sets of pre-treatments were designed. In the aging pre-treatment, the focus was solely placed on developing microstructure evolution while minimizing the creep strain by exposing the material to elevated temperatures and low-stress levels. The <001> single-crystals of CMSX-8 were all aged at 1100 ^{0} C and 130 MPa tensile axial loading for 50-60 hours to degrade the microstructure to the fully-rafted state depicted in Figure 2 (b) while the total creep deformation did not exceed 2%. The aging conditions were determined from the prior study on the kinetics of microstructure evolution of CMSX-8 [23] to assure maximal morphology change and minimal deformation. On the other hand, the creep pre-treatment on the CMSX-8 specimens was

performed with the main purpose of introducing considerable creep damage to the microstructure, increasing the density of dislocations and altering their configuration and arrangement while the morphology of the γ/γ′ structure stays intact. The creep deformation was terminated at the creep strain of 5.0-6.0% which was the onset of the tertiary creep regime at the temperature of 900 ^{0} C. According to the prior study [23], the kinetics of diffusion-controlled microstructure evolution at this temperature is substantially slow and no noticeable morphology alteration is detected. The details of the creep and aging pre-treatments are listed in Table 2.

Table 2 Conditions of the prior-treatment to the LCF testing

	Temperature (°C)	Stress (MPa)	Termination criterion
pre-aging	1100	130	t = 50-60 h
pre-creep	900	400	ε = 5.0-6.0%

The subsequent LCF experiments were carried out using MTS computer-controlled closed-loop servohydraulic testing machines in the strain-controlled mode with 100 kN (22kip) load capacity. Note that in the current sequential experiments, unlike the previous studies that both static and cyclic loading were performed in a similar mode, the creep and fatigue tests are conducted at load- and displacement-controlled modes, respectively (Figure 3 (a)). All testing was carried out with the strain amplitude of 0.5%, R_ε ratio of zero and strain rate of 10^{-3} 1/s at three different temperatures of 20 °C, 750 °C and 1100 °C to investigate the interaction at temperature regimes that the material exhibits distinct damage mechanisms. The influence of the cyclic loading type and developed mean stress was studied at 1100 °C by altering the R_ε ratio from zero to -∞. The temperature was uniformly distributed and controlled by employing induction coil and a 2 kW induction heater. The temperature measurements were carried out using K-type thermocouples welded to the gage section of the dogbone specimens. In addition, high-temperature MTS extensometers with attached alumina rods, extended in between induction coils, were employed to measure the axial displacement within the gage section.

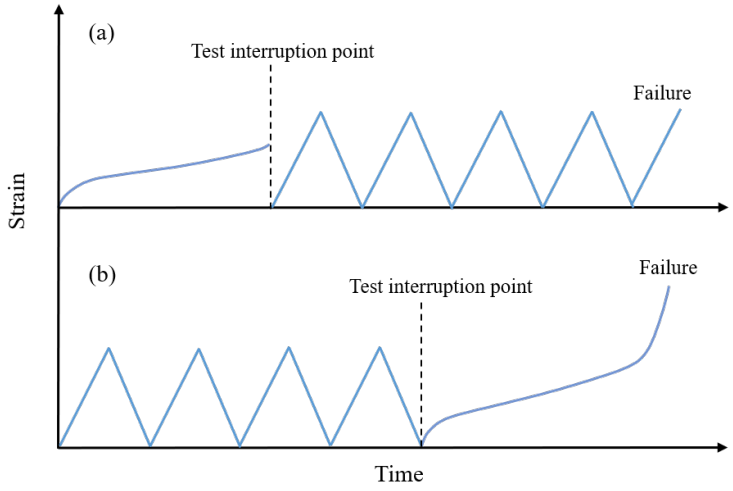

Figure 3 Schematic of the sequential loading technique.

Besides the bulk microstructure degradation that is imposed on the specimens through aging pre-treatment, a local change is observed as well in the vicinity of the free surface where the oxide layer is formed. The precipitates consist of elements that are prone to oxidation (e.g. Ni and Al). Therefore, via the inter-diffusion of such elements at elevated temperatures, the γ′ stabilizing elements travel to the free surface, be consumed by the oxide film and consequently a precipitate free zone (PFZ) is formed. The configuration of the local degradation near the free surface is illustrated in Figure 2 (c). To assure the validity of the LCF experiments according to the ASTM E606 standard for strain-controlled fatigue tests, the sample specification requires the removal of the oxide and the γ′ depleted layer from the gage section to prevent pre-mature crack initiation. The last 0.001 inch was polished with silicon paper in the longitudinal direction to avoid in-plane local stress concentration and a maximum of 0.2 μm surface roughness was imparted to the gage section.

The isothermal cyclic tests associated with hold times (CFI) were conducted in a similar manner as the LCF experiments to provide an appropriate reference to evaluate the type of interaction that can impair the fatigue resistance more severely. The duration of hold time was chosen to be 3 minutes with the position at the peak strain of 1% while the strain amplitude, R_ε ratio, and temperature were maintained to the equivalent LCF conditions.

To examine the impact of the prior cyclic loading that is exerted on the creep deformation of the superalloy, the samples were fatigued at 20 °C and 1100 ˚C, strain amplitude of 0.5% and R_ε of zero to 60% of their total fatigue life that was determined by running a similar sample geometry under the same conditions to the failure point. Subsequently, they were placed under a constant load at two temperatures of 800 ˚C and 900 ˚C and stress levels of 700 and 400 MPa. The creep loading conditions were selected such that two distinct creep curves are created. The former creep conditions at 800 ˚C highlights the influence of pre-cycling on the primary creep region while the latter time-dependent deformation response is dominated by the secondary creep regime to evaluate the creep-rupture life and creep strain rate variation.

Results and Discussions

Prior-treatment influence on the fatigue behavior

The life variation of the differently treated specimens is presented in the bar plot of Figure 4. To analyze the fatigue behavior of the samples with aged microstructure and pre-existing creep strain and compare them against the baseline fatigue and CFI behavior of as-heat-treated microstructure, the stress-strain response of the first 10 cycles has been plotted in Figure 5. It should be noted that the fatigue failure criterion is the life at which the crack reaches the critical size and an abrupt drop of stress amplitude occurs.

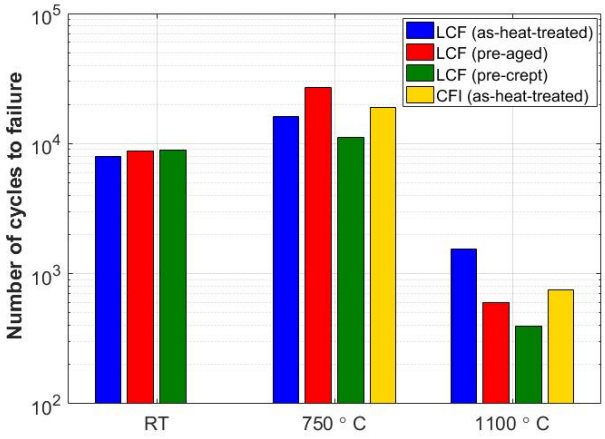

Figure 4 Effect of different types of creep and fatigue interaction on fatigue life.

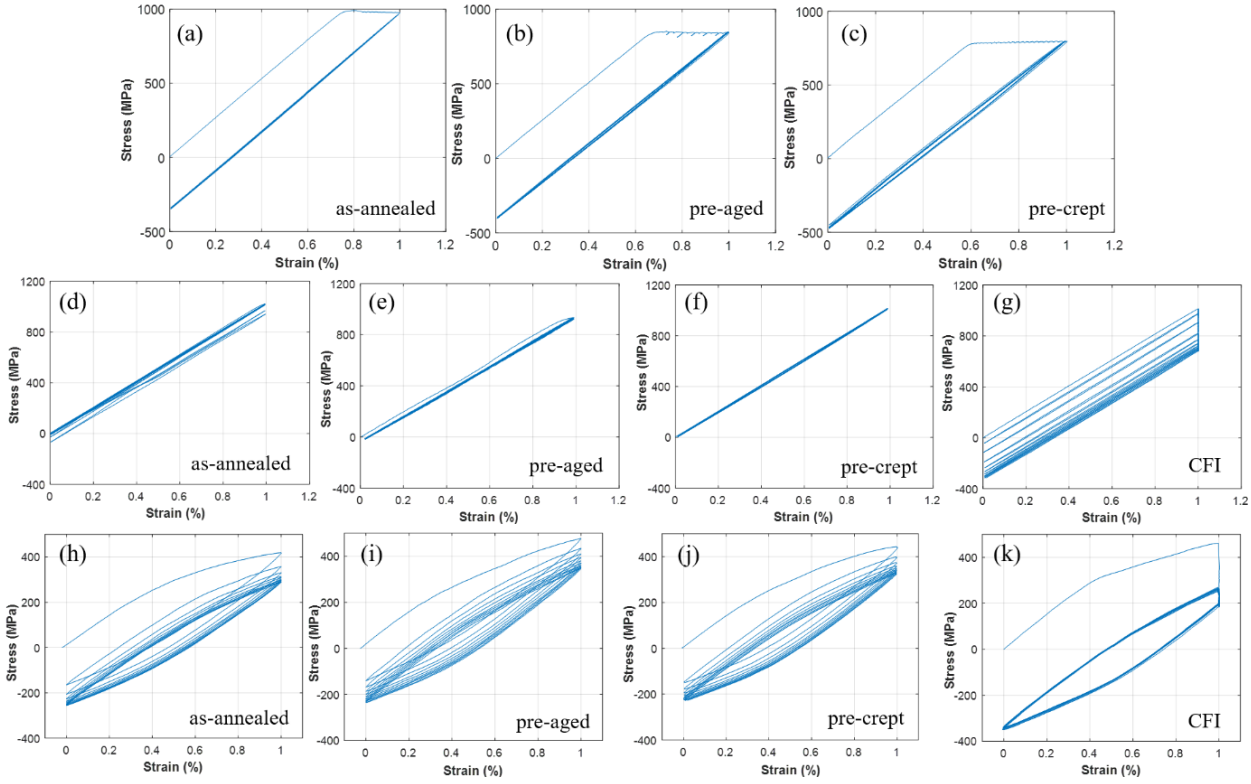

Figure 5 Stress-strain response of the as-annealed, pre-aged and pre-crept LCF and CFI tests at (a-c) 20 ˚C, (d-g) 750 ˚C, and (h-k) 1100 ˚C.

Figure 4 shows no significant variation in the life data of the tests performed at 20 °C and 750 ˚C, whereas the pre-treatments led to the substantial reduction of fatigue life at 1100 ˚C up to 74%. Thus, it appears that the effect of prior treatment and hold time is sensitive to the adopted fatigue temperature. Figure 5(a-g) shows that at the low and intermediate temperatures, under the testing conditions, CMSX-8 essentially exhibits the predominant elastic cyclic response with zero, insignificant or unmeasurably small inelastic strain that did not exceed 0.009%. Therefore, the total fatigue life is solely governed by the elastic strain amplitude and

hence rupture strength of the material becomes the deciding factor in governing the life of the specimen which hasn't shown to be influenced by the morphology or the accumulated creep strain. This observation agrees well with the corresponding life results that exhibit comparable values for different microstructures tested at 20 °C. Although the variation of the dispersed life data at 750 ˚C is high, the difference is within the scattered band of factor two. According to Mughrabi [24], such a complete elastic behavior of the hysteresis loop only occurs at stress levels lower than the material's fatigue limit. Hence, attaining the saturated stress amplitudes as high as 500 MPa and 620 MPa at 20˚C and 750˚C, implies an excellent fatigue strength of the CMSX-8 superalloy. Despite the absence of considerable cyclic inelastic strain, the cumulation of the irreversible shear strain imposed on the material over a large number of cycles is destructive and promotes crack initiation and propagation. It should be recognized that even though no meaningful influence of the dwell time, pre-deformation and microstructure on fatigue performance at low and intermediate temperature regimes under the testing conditions can be inferred from the experimental observations and the results indicate that the impact is identical at these two temperatures, the monotonic response extracted from the first cycle distinguishes the differences and highlights the effect of the microstructure.

At low temperatures, the material reaches and passes the yield point during the first cycle that is followed by cyclic loading dominated by elastic deformation. The inelastic strain at the end of the first cycle reaches up to 0.05% whereas, at 750 ˚C the material stays in the elastic regime and does not reach the yield point. One of the striking facts about Ni-base superalloys is the anomalous increase of the yield strength and UTS with raise in temperature up to intermediate temperatures, while the ductility is maintained. The remarkable strength of the material at this temperature is ascribed to the existing ordered phase in which thermally activation of the cube-slip mode takes place and contribute to the formation of the sessile obstacles and introduction of an excess hindrance to dislocation motion that promotes the dislocation entanglement [25-27]. The increase in yield stress peaks at the temperature of about 750 ˚C for CMSX-8 [21]. On the other hand, it is evident from Figure 6 that the impact of the pre-treatment at 20 °C manifests itself by the change in yield strength. Similar behavior was observed by Epishin et al. [18] for CMSX-4 where the shape of the stress-strain curve is altered by severe degradation that comprised the combined influence of microstructural degradation and creep deformation. Introduction of the prior creep strain seems to be more influential in decreasing the strength of the material than the evolution of the microstructure as it undergoes 20 % reduction from 978 MPa down to 791 MPa. Hence, it can be concluded that the impact on the monotonic stress-strain curve does not necessarily indicate the susceptibility of fatigue life and cyclic constitutive response to the pre-treatments. Moreover, it is interesting to note that analogous to the tests at 750 ˚C, all tests performed at 20˚C share equal elastic modulus which explains the invariant fatigue life at these temperature regimes.

Figure *5* (a-g) reveals no obvious indication of the cyclic hardening and softening and transition to the cyclically stable condition is achieved within the first few cycles in most cases. It is noted that the crack initiation and propagation constitute most of the fatigue life of the high strength engineering materials while the softening/hardening portion of life is negligibly small. The mean stress evolution of the LCF and CFI experiments up to the fracture point is presented in Figure 7. The absence of accumulated

inelastic strain at 20 °C and 750 ˚C during a fixed positive amplitude of cyclic strain results in maintaining the tensile mean stress while in the same plot it is shown that by subjecting the sample to hold times the mean stress relaxation takes place and tends to approach to zero. Such stress relaxation is readily recognized from the first few cycles (Figure 5 (g)) that continues until the stabilized hysteresis condition is obtained. Even though the detrimental effect of tensile mean stress on fatigue life has already been well established, in the current experimentation at 750˚C it has not ultimately led to an evident difference in fatigue life. Indeed, there are multiple contributing factors that play role in determining the total fatigue life such as hold time, mean stress, and environment that may improve or impair the performance and essentially it is the combination of such effects that has brought about comparable performance.

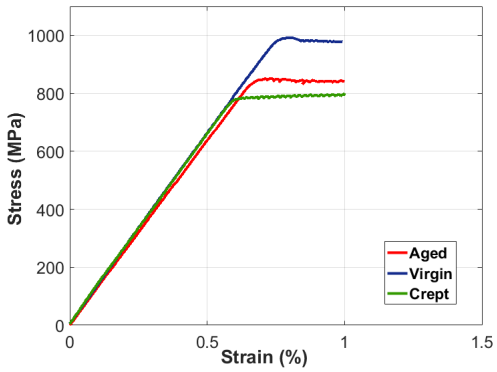

Figure 6 Influence of the microstructure on monotonic stress-strain response at 20 ˚C.

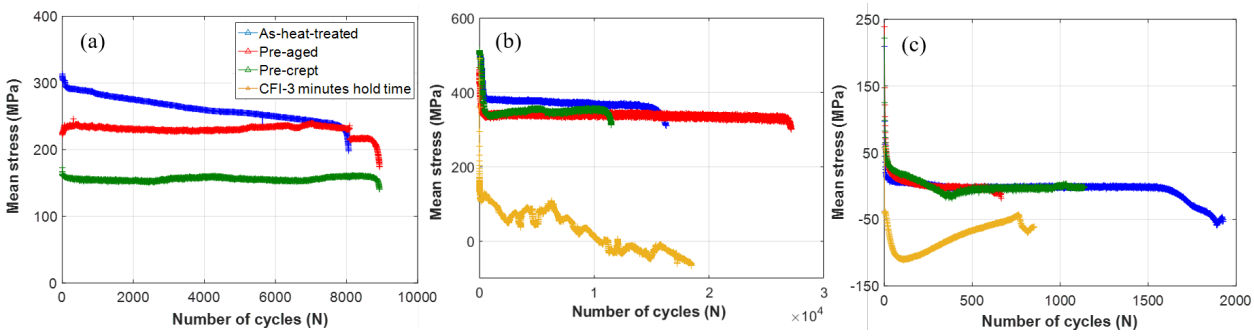

Figure 7 Mean stress evolution of the LCF and CFI tests performed at (a) 20 ˚C (b) 750 ˚C and (c) 1100 ˚C under $R_\varepsilon = 0$ condition.

On the contrary, at the highest temperature, wider hysteresis loops are formed by a significant increase in the cyclic inelastic strain range up to 0.3% (Figure 5 (h-k)). If the test is predominated by the inelastic strain amplitude, the fatigue life is dictated by ductility of the material. Accordingly, a pronounced influence of the microstructure and dwell time on cycles to failure was observed with more deteriorative influence on the samples with pre-crept microstructure. The associated stress range evolution curves of the LCF experiments (Figure 8) suggest the absence of stabilized cyclic state and display indications of softening up to the final fracture. It is essential to know that the pre-treated samples experienced a considerable amount of necking (up to 25% reduction in area) which also contributes to the decreasing trend of the cyclic stress range. The initial stress state for all tests was

in the similar range of 550-650 MPa, regardless of their microstructure. The stable state of cyclic deformation is the consequence of the balanced competition between dislocation hardening and softening owing to the increase in sessile dislocation network density and rearrangement of dislocations in such a configuration with less mobility restriction []. At the elevated temperature of 1100 ˚C, as it is seen in Figure 5 (h-j) dislocation annihilation takes part in addition to activation of climb mechanism which enables dislocation movements in the matrix phase and an overall less impeded cyclic deformation is achieved. However, the incorporation of the creep deformation in cyclic loading in CFI experiment alters the underlying mechanisms such that the stabilized state is obtained within the second cycle.

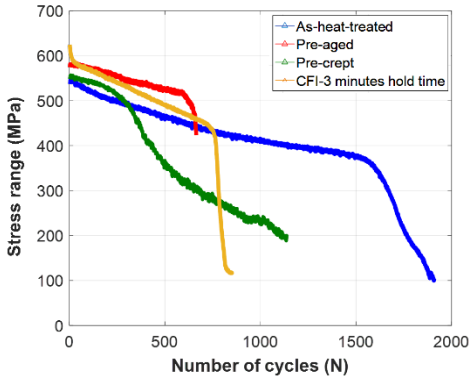

Figure 8 Stress range evolution of the LCF and CFI tests carried out at 1100 ˚C.

It is remarkable that at high temperature regimes, the decoupled influence of morphology evolution and accumulated creep strain turned out to be more degrading to the fatigue life than their combined effect as it is imposed by the CFI condition. By introducing the hold time at the peak strain of each cycle, stress relaxation occurs that leads to the development of the negative mean stress larger than 100 MPa. The compressive mean stress is known to be beneficial to fatigue life and brings about longer lives than zero and tensile mean stresses by restricting the crack tip opening and propensity to propagate [28-30]. Consequently, the adverse effect of cumulative creep strain induced by the hold time at each cycle is alleviated and results in longer life than the pre-treated samples.

A comparison is made between the literature findings on the response of the CMSX-4 superalloy and the preceding results on CMSX-8. Ott and Mughrabi [19] reported the reduced fatigue life of the CMSX-4 sample at elevated temperature regime and strain amplitude slightly higher than the value adopted in the current paper, for the N-type rafted microstructure the findings were entirely consistent and in agreement with the behavior observed for CMSX-8. They also investigated the beneficial and improving effect of the P-type rafts in prolonging the fatigue life of the material owing to the hindrance provided for the crack propagation that delays the fast growth. However, contradictory to the results presented in this paper, Epishin et al. [18] suggested the profound influence of microstructure on LCF response at the intermediate temperature of 700 ˚C. The degradation of the samples included pre-creep process at 1100 ˚C associated with fully raft formation. Therefore, the combined effect of pre-deformation and aging was

investigated. The fully reversed cyclic loading was adopted, and it was proposed that the destructive influence becomes stronger at lower temperatures which contrasts with the present examination on CMSX-8 single-crystal. Further extensive exploration of the experimentation details of the pre-treatment and LCF testing in addition to the characterization of the material microstructure is needed to discern the origin of such conflicting observations.

Many experimental and computational studies concerning the mean stress and stress/strain ratio effect on the fatigue crack propagation behavior and fatigue lives have been carried out [31-33]. The asymmetric tension-compression response of the CMSX-8 single-crystal was investigated at 1100 ˚C, the temperature at which the most pronounced role of the microstructure on the life of the material was detected. The total number of cycles to failure for the pre-treated LCF and CFI tests with strain ratio of R_ε=0 and R_ε=-∞ is plotted in Figure 9. The observations indicate that unlike the tensile cyclic loading, at the strain ratio of -∞, no notable influence of the microstructure on the fatigue life is exerted. The cyclic and monotonic stress-strain response of the various microstructures in the compression tests were approximately analogous while similar to the tensile cyclic experiments, the mean stress amplitude abruptly relaxed to zero resulting in a completely reversed stress state. Therefore, the absence of mean stress justifies the equivalent fatigue behavior of the as-heat-treated microstructure under tension and compression. Even though further investigation and experimentation is required for clarification and to draw a firm conclusion, the lack of sensitivity of the material to microstructure under negative R ratio values can be ascribed to the fatigue-environment interaction that becomes profound in temperature regimes with the highest susceptibility to the oxidation [34]. It is well understood that crack initiation and propagation of the Ni-base superalloys strongly depend upon oxidation on the surface of the alloy [35-37].

On the other hand, imposing a compressive hold time on cycles with R_ε=-∞ contribute to the generation of a distinct response compared to the one with R_ε =0 in which a tensile hold time was incorporated within each cycle. The development of the positive mean stress by introducing the creep loading at the valley strain of each cycle proved to apply a deleterious effect on the fatigue life. The combined adverse effect of the mean stress and accumulated creep damage decreases the fatigue resistance of the material by 65% while such reduction for the sample with negative mean stress but an equal absolute value of roughly 100 MPa, is 15% less. Figure 9 (b) illustrates the development and relaxation of the mean stress during CFI tests.

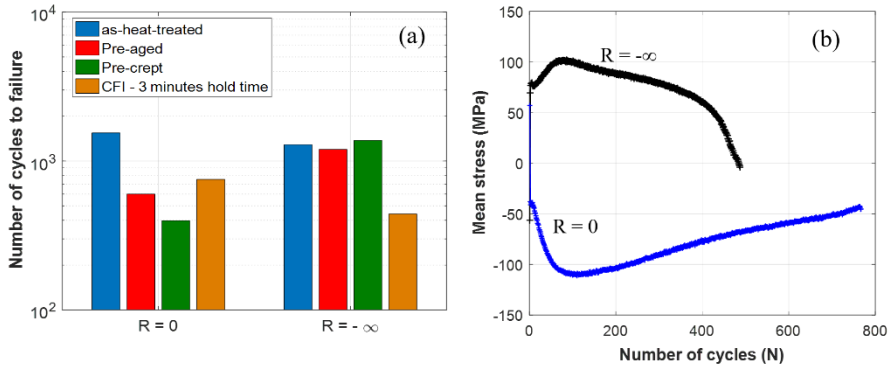

Figure 9 Influence of the strain ratio at 1100 ˚C on (a) fatigue life of the pre-treated LCF and CFI experiments and (b) CFI mean stress distribution.

Figure 10 reveals the fractography of the failed fatigued specimens at the temperature regimes of interest for the as-heat-treated and pre-crept microstructures. The examination of the fracture surface was carried out using scanning electron microscope (SEM). The crack initiation site for the tests performed at 1100 ^{0} C except Figure 10 (a), is at the sample surface. The material is prone to severe oxidation at the elevated temperature and formation of the γ' depleted zones is promoted around surface defects such as micropores which gives rise to the growth of small cracks [38]. By a cursory glance at the side view of the fracture surfaces, two types of fracture mode are identified: (i) Crystallographic fracture by which the fatigue failure takes place by the strongly localized shearing along {111} planes and (ii) planar fracture normal to the loading direction on (001) plane. At 20˚C, the crack propagation has occurred on at least two {111} planes, resulting in ±45˚ fracture surface appearance. No sign of mode change was revealed as a result of pre-treatment. Even though, the as-heat-treated sample exhibited larger {111} facets. By increasing the temperature to 750˚C, the fracture model changes to planar for both microstructures. The interesting phenomenon at this temperature is the internal crack initiation, its propagation to a critical size equivalent to the diameter of the circular-shape region, depicted in Figure 10 (c-d) and the final fast brittle-like fracture on (001) plane. At 750˚C, the strength of the superalloy is at its peak value. The absence of the inelastic strain and high resolved shear stress result in flat fracture surface with the characteristics of brittle fracture. The number of cycles to failure of the pre-crept microstructure was shown to be 30% lower than the as-heat-treated one. The justification can be made by looking at the significantly smaller fatal crack size before fast fracture. The damage introduced to the microstructure by the adopted pre-treatment may include debonding of the inclusions and formation of micro-cracks throughout the thickness that eventually will reduce the fracture toughness, leading to less resistance. The crystallographic mode of fracture is activated by increasing the temperature further to 1100˚C for as-heat-treated microstructures with R_ε = 0 and -∞. However, in the R_ε = 0 condition, the fracture mode change is observed in the pre-crept sample. The crystallographic fracture is altered to planar while associated with substantial visible necking featured by approximately 25% reduction in area at the fracture point. It was discussed earlier that such mode transition was associated with significant reduction in fatigue life. Knowing that the testing at 1100˚C under R_ε = -∞ condition involved no variation in cycles to failure and fracture mode change it is concluded that a direct correlation exists

between microstructure and fatigue life if the fracture mode is altered. The fatigue striations formed at this temperature are illustrated in Figure 11.

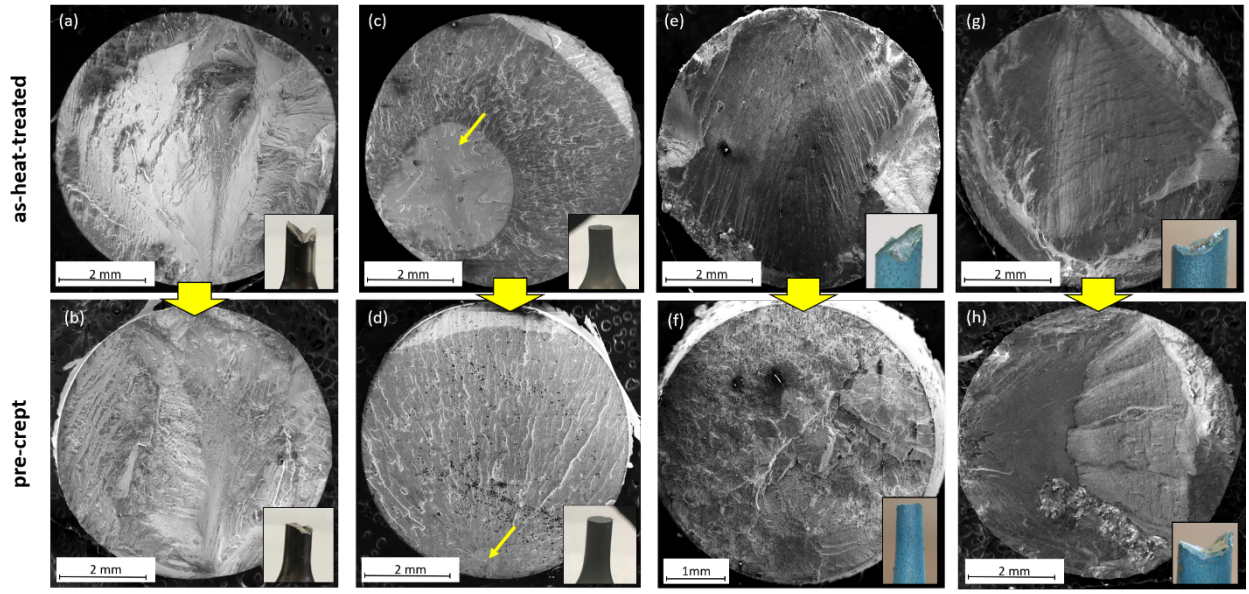

Figure 10 Fractography of the LCF failed samples tested at three temperature regimes (a-b) 20˚C, (c-d) 750˚C (e-f) 1100˚C, R_ε = 0, and (g-h) 1100˚C, R_ε = -∞.

The described observations of the fractography study along with the fatigue performance results can also be explained by the active deformation mechanisms. It is known that the size of the γ′ precipitates, the anti-phase boundary energy that has a direct correlation with temperature, and the strength of the γ′ phase which shows an anomalous increase with temperature, determine the deformation mechanism energetically favored by dislocations and the crystallographic plane on which failure occurs [39, 40]. At low temperatures, the primary and dominant deformation mechanism in Ni-base superalloys is the shear of the γ′ precipitates by the dislocation ribbons including dislocation pairs of overall burgers vector of $a < 112 >$ which form and remove anti-phase boundaries (APB) as they travel through the ordered structure of the γ′ precipitates [40, 41]. The low strength of the γ′ phase at 20 ˚C imposes less resistance towards dislocation movement. Thus, both γ and γ′ contribute to the deformation occurring on {111} planes. The anomaly in the increase of the ordered precipitate's strength with temperature alters the mechanism. The failure will be confined to the matrix phase. Dislocations tend to loop around the particles and since the thermally-induced climb of screw dislocations has been facilitated, the $\langle 110 \rangle \{111\}$ slip systems in γ matrix are activated, and the deformation mechanism is dominated by the glide and climb of dislocations in the matrix [5, 42]. The localized deformation that is restricted to the γ channels brings about a fracture surface perpendicular to the direction of stress axis at 750 ˚C. With raising the temperature beyond, the strength of the γ′ particles is lowered. Hence, the precipitates are not regarded as obstacles that impede the glide of the dislocations

and crystallographic fracture surface is attained due to the deformation in both matrix and particles. However, the introduction of the creep damage to the microstructure and formation of voids, microcracks and debonding of inclusions eventuate to (001) fracture surface.

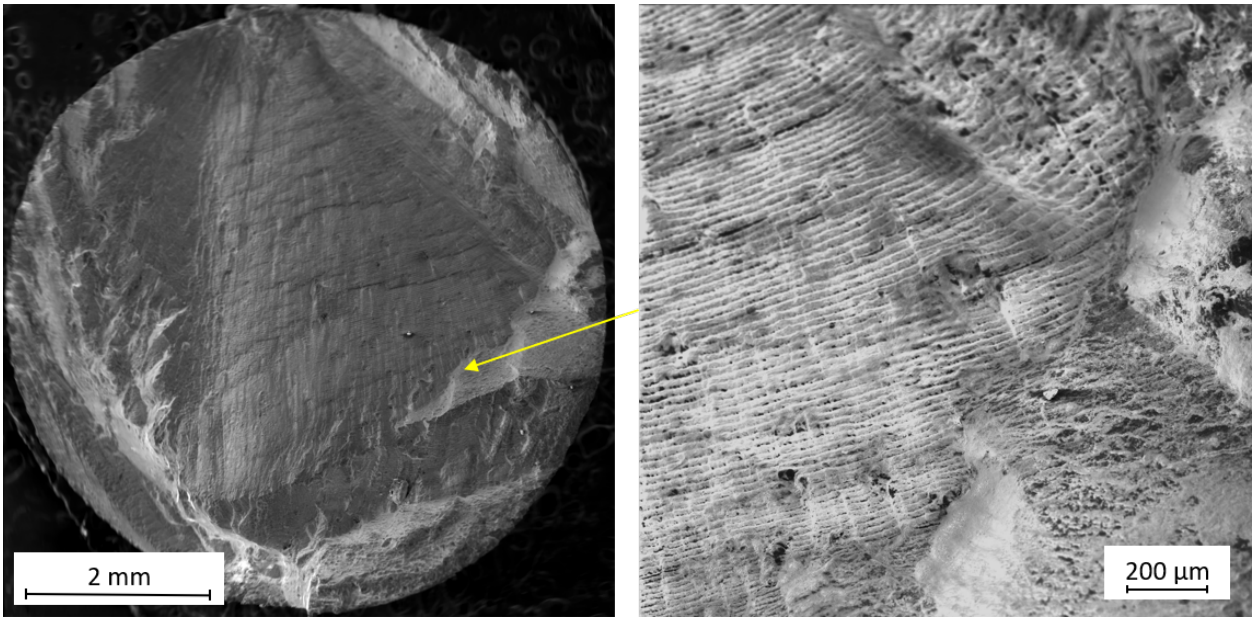

Figure 11 Fatigue striations formation at 1100 ˚C.

Prior-fatigue influence on the creep behavior

The temperature and stress conditions required to act on the material for the activation of the rafting, tertiary and primary creep modes have been identified for CMSX-4 single-crystals [5]. Although the lower Re content of the CMSX-8 exacerbates the creep susceptibility, there is no considerable deviation between the creep behavior of the two superalloys, particularly at low temperatures and high-stress levels. Therefore, the creep test conditions for the CMSX-8 superalloy were selected accordingly. The creep-rupture curves of the as-heat-treated and pre-fatigued specimens are compared in Figure 12. A distinct creep curve type is clearly distinguishable for each testing condition. At the condition of 800˚C and 700 MPa, given that the applied load is sufficiently high, the onset of creep deformation is within the primary regime. Thereafter, the creep strain rate decreases, and a hardening effect is operative with further deformation which leads to invariant strain rate during the secondary creep regime. Reduction of the stress to 400 MPa at the higher temperature of 900˚C gives rise to the tertiary creep regime that constitutes the majority of the creep life. The initial accelerated strain during primary creep is eliminated while a fast transition from the secondary creep plateau to the tertiary creep takes place.

The CMSX-8 single-crystals experienced cyclic loading to 60% of their fatigue life to induce sufficient damage and gain informative results of the interaction of creep and fatigue processes. The selected low- and high-temperature pre-fatiguing conditions enable one to examine the influence of two distinct dislocation arrangements due to the unique mechanisms operated at either of these temperature regimes. After pre-deforming the specimens at 20˚C, no clear indication of the crack formation was detectable on the surface. However, slip bands of 45˚ generated from the highly localized deformation were evidently identifiable. On the other hand, after pre-fatigue step at 1100 ˚C surface cracks were observed at the gage section of the specimen. High-temperature cyclic loading involves the accumulation of irreversible inelastic strains. The raised anti-phase boundary energy and activation of the climb and cross-slip allow dislocations to glide out of their original plane while low-temperature fatigue mechanism involves shearing of the precipitates and movement of dislocations in both phases of the γ/γ' structure.

Figure 12 demonstrates that pre-cycling the samples at 20 ˚C exerts no impact on the secondary and tertiary regimes of the creep response. In addition, ductility and steady-state creep rate of the material have maintained the values of the as-heat-treated microstructure. However, the influence on primary creep regime at 800 °C is apparent. Cyclic deformation, particularly at higher temperatures that is associated with significant inelastic strain, increases the density of dislocations and alters their configurations in such a way that they become tangled and form barriers at locations such as phase boundaries. The entanglement of the dislocations contributes to the reduction of the primary creep strain by introducing hindrance to the facilitated movement of the dislocations during primary creep. Although similar argument and reasoning can be applicable to the high-temperature pre-fatigued samples, the extent of damage that material has experienced leads to the elimination of the primary and secondary creep and the onset of the tertiary regime that progresses until terminated by the catastrophic rupture of the material at fraction of the total creep-rupture life of the as-heat-treated material. At lower stress level of 400 MPa, even though the damage accumulation did not change the creep rate, the ductility is affected remarkably, and the total life is reduced by 80%. As was expected, the results suggest that the pre-deformation at 1100 °C is more detrimental to the creep behavior. At 20 °C, the dislocations perform small forward and backward movements that due to their primary elastic nature is less damaging. Additionally, at the creep conditions that activate primary creep, higher sensitivity to the pre-deformation is observed. The results suggest that lower temperature and higher stress creep conditions are more susceptible to the prior-fatigue deformation. This is in agreement with the findings on influence of different microstructural conditions developed by various heat treatments on creep properties of STAL-15 Ni-base superalloy [43].

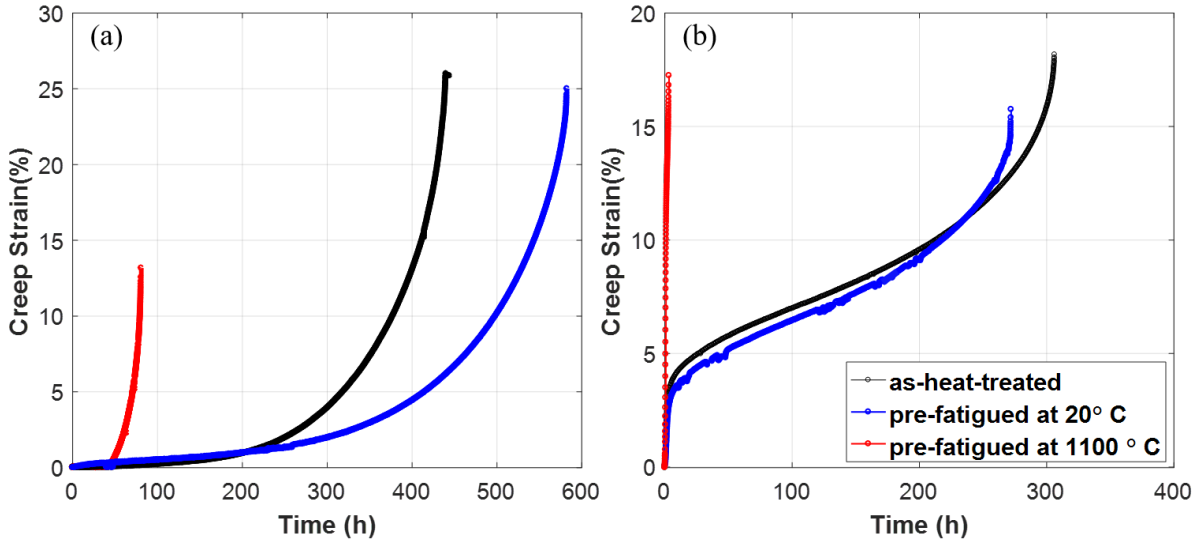

Figure 12 Creep-rupture curves of the samples with as-heat-treated and pre-fatigued microstructure at temperatures and sustained stresses of (a) 900°C and 400 MPa (b) 800°C and 700 MPa.

Conclusions

The decoupled influence of prior creep and fatigue deformation on subsequent fatigue and creep response of a second-generation Ni-base superalloy was studied while the independent role of morphological degradation and creep inelastic strain on fatigue was explored. Based on the accomplished experimental study the following conclusions are made:

1. The creep-fatigue interaction of the CMSX-8 superalloy is deduced to be highly temperature sensitive. The pre-creep deformation showed to reduce the yield and tensile strength at 20 ^{0} C while LCF behavior is unaffected. Even though the purely elastic response at the peak strength of 750 ˚C didn't confer a strong influence of pre-treatment on fatigue response, the fracture surface appearance signified the reduction in propagated crack size before final fatal fracture. The LCF properties exhibited the highest sensitivity to the microstructure and inelastic deformation at 1100 ˚C with the factor of 4, demonstrating the higher contribution of the accumulated creep strain in deteriorating fatigue life comparing to microstructural changes. In addition, the more enhanced detrimental effect was observed compared to the CFI condition with the incorporation of the tensile hold time. Moreover, no notable creep influence was exerted at such high temperature when the R_{ε} changed from zero to -∞ presuming that the fatigue-environment interaction becomes more important.
2. The fractographic studies suggested that the pronounced effect of the prior-treatment on the LCF properties is associated with fracture mode change. By introducing the microstructural degradation and creep strain to the material, the localized crystallographic fracture on {111} planes transited to more homogeneous deformation accompanied by extensive necking leading to fracture surface normal to loading axis. At low- and high-temperatures the Ni-base superalloy is prone to

crystallographic fracture on one or more {111} planes while at intermediate temperatures that the brittle-type fracture is promoted due to peak strength the fracture surface exhibits flat appearance.

3. Prior-cycling at 1100 ˚C accumulated more damage than 20 ˚C pre-fatiguing that brought about substantial creep-rupture life reduction. The adverse influence resulted in the onset of the accelerated tertiary creep as the only activated creep regime or an escalated transition from secondary to tertiary depending on the creep conditions. The reconfiguration and increase in dislocation density turned out to reduce the primary creep region by restricting the high-rate progressive deformation while in both cases the steady-state creep rate during secondary regime maintained invariant. Overall, the fatigue deformation proved to be more influential on the low temperature and high stress creep conditions.

Acknowledgements

This work is supported by U.S. Department of Energy, National Energy Technology Laboratory, University Turbine Systems Research (UTSR) Program, Grant DE-FE0011722, and Siemens Energy Inc., Orlando, FL.

References

[1] A. Pineau and S. D. Antolovich, "High temperature fatigue of nickel-base superalloys – A review with special emphasis on deformation modes and oxidation," *Engineering Failure Analysis,* vol. 16, no. 8, pp. 2668-2697, 2009/12/01/ 2009.

[2] K. Singh, "Advanced Materials for Land Based Gas Turbines," *Transactions of the Indian Institute of Metals,* vol. 67, no. 5, pp. 601-615, 2014/10/01 2014.

[3] A. M. Ibrahim Dincer, Haydar Kucuk, *Progress in Sustainable Energy Tehcnologies: Generating Renewable Energy*. 2014.

[4] K. H. J.B.Wahl, "Advances in Single Crystal Superalloys - Control of Critical Elements " in *7th Parsons conference*, 2007.

[5] R. C. Reed, *The superalloys* 1st ed. Cambridge University press, 2006.

[6] D. Hu and R. Wang, "Experimental study on creep–fatigue interaction behavior of GH4133B superalloy," *Materials Science and Engineering: A,* vol. 515, no. 1, pp. 183-189, 2009/07/25/ 2009.
[7] S. X. Li and D. J. Smith, "High temperature fatigue-creep behaviour of single crystal SRR99 nickel-base superalloys: part II - fatigue-creep life behaviour " *Fatigue & Fracture of Engineering Materials & Structures,* vol. 18, no. 5, pp. 631-643, 1995.
[8] J. P. Pédron and A. Pineau, "The effect of microstructure and environment on the crack growth behaviour of Inconel 718 alloy at 650 °C under fatigue, creep and combined loading," *Materials Science and Engineering,* vol. 56, no. 2, pp. 143-156, 1982/11/01/ 1982.
[9] C. J. Pierce, A. N. Palazotto, and A. H. Rosenberger, "Creep and fatigue interaction in the PWA1484 single crystal nickel-base alloy," *Materials Science and Engineering: A,* vol. 527, no. 29, pp. 7484-7489, 2010/11/15/ 2010.
[10] R. V. Miner, J. Gayda, and R. D. Maier, "Fatigue and creep-fatigue deformation of several nickel-base superalloys at 650 °c," *Metallurgical Transactions A,* vol. 13, no. 10, pp. 1755-1765, 1982/10/01 1982.
[11] B. Fournier *et al.*, "Creep–fatigue–oxidation interactions in a 9Cr–1Mo martensitic steel. Part I: Effect of tensile holding period on fatigue lifetime," *International Journal of Fatigue,* vol. 30, no. 4, pp. 649-662, 2008/04/01/ 2008.
[12] T. Billot, P. Villechaise, M. Jouiad, and J. Mendez, "Creep–fatigue behavior at high temperature of a UDIMET 720 nickel-base superalloy," *International Journal of Fatigue,* vol. 32, no. 5, pp. 824-829, 5// 2010.
[13] J. Zrník, J. Semeňák, V. Vrchovinský, and P. Wangyao, "Influence of hold period on creep–fatigue deformation behaviour of nickel base superalloy," *Materials Science and Engineering: A,* vol. 319–321, pp. 637-642, 12// 2001.
[14] A. Epishin, T. Link, H. Klingelhöffer, B. Fedelich, and P. Portella, "Creep damage of single-crystal nickel base superalloys: mechanisms and effect on low cycle fatigue," *Materials at High Temperatures,* vol. 27, no. 1, pp. 53-59, 2010/03/01 2010.
[15] H. Mughrabi and U. Tetzlaff, "Microstructure and High-Temperature Strength of Monocrystalline Nickel-Base Superalloys," *Advanced Engineering Materials,* vol. 2, no. 6, pp. 319-326, 2000.
[16] F. R. N. Nabarro, "Rafting in superalloys," (in English), *Metallurgical and Materials Transactions a-Physical Metallurgy and Materials Science,* Article vol. 27, no. 3, pp. 513-530, Mar 1996.
[17] T. M. Pollock and A. S. Argon, "Directional coarsening in nickel-base single crystals with high volume fractions of coherent precipitates," *Acta Metallurgica et Materialia,* vol. 42, no. 6, pp. 1859-1874, 1994/06/01/ 1994.
[18] A. Epishin, T. Link, M. Nazmy, M. Staubli, H. Klingelhoffer, and G. Nolze, "Microstructural degradation of CMSX-4: Kinetics and effect on mechanical properties," (in English), *Superalloys 2008,* Proceedings Paper pp. 725-731, 2008.
[19] M. Ott and H. Mughrabi, "Dependence of the high-temperature low-cycle fatigue behaviour of the monocrystalline nickel-base superalloys CMSX-4 and CMSX-6 on the γ/γ′-morphology," *Materials Science and Engineering: A,* vol. 272, no. 1, pp. 24-30, 11/15/ 1999.
[20] J. B. W. Ken Harris, "Improved Single Crystal Superalloys, CMSX-4 (SLS)[La+Y] and CMSX-486," in *Superalloys*, Seven Springs, PA, USA, 2004.
[21] J. B. Wahl and K. Harris, "New single crystal superalloys, CMSX (R)-7 and CMSX (R)-8," (in English), *Superalloys 2012,* Proceedings Paper pp. 179-188, 2012.
[22] Y. K. T. Murakumo, K. Kobayashi and H. Harada, "Creep Strength of Ni-base Single-crystal Superalloys on the gamma/gamma' Tie-line," in *Superalloys*, Seven Springs, PA, USA, 2004.
[23] E. A. E. R. S. Gorgannejad, R.W. Neu, "Ageing kinetics of Ni-base superalloys," *Materials at High Temperatures,* vol. 33, no. 4-5, pp. 291-300, 2016.
[24] H. Mughrabi, "Microstructural mechanisms of cyclic deformation, fatigue crack initiation and early crack growth," (in eng), *Philos Trans A Math Phys Eng Sci,* vol. 373, no. 2038, Mar 28 2015.
[25] D. M. S. D. N. Duhl, "The effect of orientation, temperature and Gamma prime size on the yield strength of a single crystal Nickel base superalloy," in *Superalloys*, Seven Springs Mountain Resort, Champion, Pennsylvania, 1984: Metallurgical Society of AIME.
[26] Y. M. Wang-Koh, "Understanding the yield behaviour of L12-ordered alloys," *Materials Science and Technology,* vol. 33, no. 8, pp. 934-943, 2017/05/24 2017.
[27] P. Veyssière, "Yield stress anomalies in ordered alloys: a review of microstructural findings and related hypotheses," *Materials Science and Engineering: A,* vol. 309-310, pp. 44-48, 2001/07/15/ 2001.
[28] S. K. Koh and R. I. Stephens, "Mean stress effects on low cycle fatigue for a high strength steel," *Fatigue & Fracture of Engineering Materials & Structures,* vol. 14, no. 4, pp. 413-428, 1991.
[29] L. Susmel, R. Tovo, and P. Lazzarin, "The mean stress effect on the high-cycle fatigue strength from a multiaxial fatigue point of view," *International Journal of Fatigue,* vol. 27, no. 8, pp. 928-943, 2005/08/01/ 2005.
[30] E. Vacchieri, A. Costa, A. Riva, E. Poggio, and S. R. Holdsworth, "Creep-fatigue interactions in equiaxed and single crystal Ni-base superalloys," *MATEC Web of Conferences,* 10.1051/matecconf/20141419002 vol. 14, // 2014.
[31] S. Ishihara, A. J. McEvily, M. Sato, K. Taniguchi, and T. Goshima, "The effect of load ratio on fatigue life and crack propagation behavior of an extruded magnesium alloy," *International Journal of Fatigue,* vol. 31, no. 11, pp. 1788-1794, 2009/11/01/ 2009.
[32] X. Huang and T. Moan, "Improved modeling of the effect of R-ratio on crack growth rate," *International Journal of Fatigue,* vol. 29, no. 4, pp. 591-602, 2007/04/01/ 2007.
[33] N. E. Dowling, "Mean stress effects in strain–life fatigue," *Fatigue & Fracture of Engineering Materials & Structures,* vol. 32, no. 12, pp. 1004-1019, 2009.

[34] R. L. A. Stephen D. Antolovich, Richard W. Neu, A Staroselsky, "On the Development of Physically Based Life Prediction Models in the Thermo Mechanical Fatigue of Ni-Base Superalloys," *Key Engineering Materials,* vol. 465, pp. 47-54, 2011.
[35] E. Andrieu, R. Molins, H. Ghonem, and A. Pineau, "Intergranular crack tip oxidation mechanism in a nickel-based superalloy," *Materials Science and Engineering: A,* vol. 154, no. 1, pp. 21-28, 1992/06/01/ 1992.
[36] R. Molins, G. Hochstetter, J. C. Chassaigne, and E. Andrieu, "Oxidation effects on the fatigue crack growth behaviour of alloy 718 at high temperature," *Acta Materialia,* vol. 45, no. 2, pp. 663-674, 1997/02/01/ 1997.
[37] R. W. Neu and H. Sehitoglu, "Thermomechanical fatigue, oxidation, and Creep: Part II. Life prediction," *Metallurgical Transactions A,* vol. 20, no. 9, pp. 1769-1783, 1989/09/01 1989.
[38] S. A. K. H. Mughrabi, "Thermo-mechanical fatigue of the monocrystalline Nickel-base superalloy CMSX-6," presented at the ASTM International, 1996.
[39] J.-F. Huang *et al.*, "Molecular dynamics simulation of persistent slip bands formation in nickel-base superalloys," *International Journal of Automation and Computing,* vol. 14, no. 1, pp. 68-79, 2017/02/01 2017.
[40] V. A. Vorontsov, C. Shen, Y. Wang, D. Dye, and C. M. F. Rae, "Shearing of γ′ precipitates by a ⟨112⟩ dislocation ribbons in Ni-base superalloys: A phase field approach," *Acta Materialia,* vol. 58, no. 12, pp. 4110-4119, 2010/07/01/ 2010.
[41] B. Reppich, "Some new aspects concerning particle hardening mechanisms in γ' precipitating Ni-base alloys—I. Theoretical concept," *Acta Metallurgica,* vol. 30, no. 1, pp. 87-94, 1982/01/01/ 1982.
[42] I. S. Kim, B. G. Choi, J. E. Jung, J. Do, and C. Y. Jo, "Effect of microstructural characteristics on the low cycle fatigue behaviors of cast Ni-base superalloys," *Materials Characterization,* vol. 106, pp. 375-381, 2015/08/01/ 2015.
[43] A. Sato, J. J. Moverare, M. Hasselqvist, and R. C. Reed, "On the Mechanical Behavior of a New Single-Crystal Superalloy for Industrial Gas Turbine Applications," *Metallurgical and Materials Transactions A,* vol. 43, no. 7, pp. 2302-2315, 2012/07/01 2012.

APPENDIX 2

CRYSTAL VISCOPLASTICITY MODEL FOR THE CREEP-FATIGUE INTERACTIONS IN SINGLE-CRYSTAL NI-BASE SUPERALLOY CMSX-8

Ernesto A. Estrada Rodas[1] and Richard W. Neu[1,2]

[1]The George W. Woodruff School of Mechanical Engineering, Georgia Institute of Technology, Atlanta GA

[2]School of Materials Science and Engineering, Georgia Institute of Technology, Atlanta, GA

ABSTRACT

A crystal viscoplasticity (CVP) model for the creep-fatigue interactions of nickel-base superalloy CMSX-8 is proposed. At the microstructure scale of relevance, the superalloys are a composite material comprised of a γ phase and a γ' strengthening phase with unique deformation mechanisms that are highly dependent on temperature. Considering the differences in the deformation of the individual material phases is paramount to predicting the deformation behavior of superalloys at a wide range of temperatures. In this work, we account for the relevant deformation mechanisms that take place in both material phases by utilizing two additive strain rates to model the deformation on each material phase. The model is capable of representing the creep-fatigue interactions in single-crystal superalloys for realistic 3-dimensional components in an Abaqus User Material Subroutine (UMAT). Using a set of material parameters calibrated to superalloy CMSX-8, the model predicts creep-fatigue, fatigue and thermomechanical fatigue behavior of this single-crystal superalloy. Finally, a sensitivity study of the material parameters is done to explore the effect on the deformation due to changes in the material parameters relevant to the microstructure.

NOMENCLATURE

b	Burgers vector magnitude
C_{44}	*44* Component of the crystallographic elastic tensor in Voigt notation
$\chi_{\gamma}^{(\alpha)}$	Backstress in the γ phase in the α^{th} slip system
δ	Lattice misfit parameter
F_{attack}	Debye frequency
f_{γ}	Volume fraction of the γ phase
$f_{\gamma'}$	Volume fraction of the γ' phase
$\dot{\mathbf{F}}^{in}$	Inelastic deformation gradient rate
G	Bulk shear modulus as a function of temperature
γ_{APB}	Antiphase boundary energy
$\dot{\gamma}_{\gamma}^{in(\alpha)}$	Inelastic strain rate in the γ phase on the α^{th} slip system
$\dot{\gamma}_{L1_2}^{in(\alpha)}$	Inelastic strain rate in the γ' phase on the α^{th} slip system
k	Boltzmann constant
$\kappa_{\gamma}^{(\alpha)}$	Threshold stress in the γ phase on the α^{th} slip system
$\kappa_{L1_2}^{(\alpha)}$	Threshold stress in the γ' phase on the α^{th} slip system
$\lambda_{\gamma}^{(\alpha)}$	Average dislocation spacing in the γ phase on the α^{th} slip system
$\lambda_{L1_2}^{(\alpha)}$	Average dislocation spacing in the γ' phase on the α^{th} slip system
L_{γ}	γ phase channel width
$L_{\gamma'}$	γ' precipitate size
$\mathbf{L}^{in}$	Inelastic velocity gradient
$L_{\rho}^{(\alpha)}$	Average spacing of forest dislocations on the α^{th} slip system
n	Strain sensitivity exponent
N_{slip}	Number of slip systems
Q_{slip}^{110}	Activation energy for slip in the γ phase
Q_{slip}^{112}	Activation energy for slip in the γ' phase
$\rho_{F}^{(\alpha)}$	Forest dislocation density in the γ phase on the α^{th} slip system
$\rho_{\gamma}^{(\alpha)}$	Dislocation density in the γ phase on the α^{th} slip system

$\rho_{Ll_2}^{(\alpha)}$	Dislocation density in the γ' phase on the α^{th} slip system
$\rho_{P}^{(\alpha)}$	Parallel dislocation density in the γ phase on the α^{th} slip system
$\rho_{P_{pb}}^{(\alpha)}$	Parallel dislocation density in the γ/γ' interphase (phase boundary) on the α^{th} slip system
$\rho_{pb}^{(\alpha)}$	Dislocation density in the γ/γ' interface (phase boundary) on the α^{th} slip system
T_{melt}	Melting temperature of the γ phase
τ_{APB}	Antiphase boundary resistance
$\tau_{eff_{\gamma}}^{(\alpha)}$	Effective resolved shear stress in the γ phase on the α^{th} slip system
$\tau_{eff_{\gamma'}}^{(\alpha)}$	Effective resolved shear stress in the γ' phase on the α^{th} slip system
$\tau_{\gamma pass}^{(\alpha)}$	Dislocation passing stress in the γ phase on the α^{th} slip system
$\tau_{Ll_2 pass}^{(\alpha)}$	Passing stress in the γ' phase on the α^{th} slip system
$\tau_{mis}^{(\alpha)}$	Misfit stress on the α^{th} slip system
Θ	Diffusivity parameter
$V_{c1}^{(\alpha)}$	Activation volume in the γ phase on the α^{th} slip system
$V_{c2}^{(\alpha)}$	Activation volume the γ' phase on the α^{th} slip system

1. INTRODUCTION

Aero-engines and Industrial Gas Turbines (IGTs) are used in many industries to generate power. Their usage is wide and can range from powering aircraft and large naval vessels, to generating electricity at power plants. With the continuous push for greater thermodynamic efficiency, higher temperatures are constantly being required at the hot gas path (Gurrappa and Rao 2006, Perepezko 2009). This requirement produces an increasingly hostile environment for turbine components. The turbine blades, which are responsible for extracting the work from the working fluid, are in direct contact with this hostile environment where stress and strain fields are complex, and temperatures can be above the melting temperature of the blade material (Padture et al. 2002, Gurrappa and Rao 2006). To achieve these extreme temperatures, turbine blade designers recur to the usage of advanced alloys, special thermal coatings, and specially designed turbine blades with internal cooling passages. All of the above promote several types of damage mechanisms that arise from oxidation and corrosion, diffusion, thermomechanical loading, and the kinetics of microstructure evolution whose interactions in the superalloys are intricate and to this date not well understood (Epishin et al. 2008, Epishin et al. 2010, Neu and Smith 2011, Antolovich 2015, Kontis et al. 2016).

Traditionally, turbine blades have been made of nickel-base superalloys due to their excellent high temperature properties. IGTs manufacturers are considering using single-crystal blades made of second generation superalloys commonly used in aerospace propulsion systems. This is because eliminating grain boundaries improves creep behavior (Reed 2006, Pineau and Antolovich 2009). In the development of these alloys, the focus has primarily been placed on creep performance and conventionally this has been used as the design metric for new alloys (Reed 2006, Wahl and Harris 2012). However, during operation, components are not only subject to creep but also to thermomechanical loads during the engine start-up and shut-down. Therefore, the conditions inside

IGTs and aero-engines require the understanding of creep, fatigue and their interaction. Insufficient knowledge on the material behavior often forces designers to impose large safety factors and strict inspection and replacement intervals which can be costly and inefficient.

Constitutive models offered in commercially available finite element solvers, such as Ansys and Abaqus, are limited to non-interaction creep and plasticity which do not explicitly describe the complex relationships of the interaction of the dislocations with the precipitates necessary to capture the intricate creep-fatigue interactions. Consequently, motivated by improving the prediction of mechanical behavior of superalloys, multiple authors have proposed Crystal Viscoplasticity (CVP) models that consider aspects of the microstructure of the superalloys (Ma et al. 2008, Cormier and Cailletaud 2010, Fedelich et al. 2012, Zhu et al. 2012, le Graverend et al. 2014). The model by Cormier and Cailletaud was limited to modeling creep because it ignored kinematic hardening which is essential to model stress reversals. Fedelich et al., Zhu et al. and le Graverend do consider kinematic hardening, however they only model high temperatures focusing on climb and glide of dislocations in the $\langle 001 \rangle \{111\}$ slip systems while ignoring the lower temperature shearing of γ' precipitates. Furthermore, except for the model developed by Ma et al., a shortcoming of these models is that they do not explicitly account for the deformation of the γ and γ' material phases, or that they require meshing of the microstructure and complex homogenization methods to be able to model the distinct deformation mechanisms of each material phase. The model presented by Ma et al. incorporated several physically-motivated internal state variables (ISVs), and partitioned the deformation of the γ and γ' phases. While the formulation of this model is conceptually fully 3-D, it was only implemented and verified with uniaxial stress-control creep loading and did not account for reversals of the loading. Modeling the creep-fatigue interactions in the start-up, sustained operation, and shut-down cycles in turbine components requires displacement-controlled boundary conditions and the consideration of stress and strain reversals.

In this paper, the Ma et al. model (Ma et al. 2008) is extended and implemented in a displacement-based integration code to capture this creep-fatigue coupling. A backstress and its evolution is added to provide for kinematic hardening to account for the Bauschinger effect during load reversals, a strain rate sensitivity exponent is added to model changes in strain rate during cyclic loading excursions, and the evolution of dislocations at the γ/γ' phase boundary is included to better model the process of dislocations forming in the γ channels and then piling-up at the interface before shearing the γ' precipitates. Although the CVP model proposed in this work is to an extent phenomenological, it considers several physically-based arguments to account for the distinctly different deformation mechanisms that take place in the γ phase, γ' phase, and the γ/γ' interfaces. The aim is to connect the structure and property linkages through a CVP model that can be implemented directly at the component level in a displacement-based Abaqus User Material subroutine (UMAT). In this work CMSX-8, a reduced rhenium (Re) single-crystal Ni-base superalloy, is used to calibrate the material parameters of the model. This lower-cost modification of a second-generation superalloy is relevant for IGT applications that require considerably larger blades (Wahl and Harris 2012). The CVP model is demonstrated using the new UMAT by performing several numerical experiments in which some microstructure parameters are varied and the effects of these variations on the creep-fatigue response of the superalloys are examined.

2. BACKGOUND ON THE DEFORMATION MECHANISMS SUPERALLOYS

Superalloys are comprised of an intermetallic $L1_2$ γ' strengthening phase held together by a disordered γ phase (Sabol and Stickler 1969). When dislocations meet a γ' precipitate they can either shear it or loop around it and whether one or the other takes place is dependent on the size and volume fraction of the γ' precipitates (Huther and Reppich 1978). Shearing of the γ' particles by dislocations is favored by small

precipitates, high volume fraction, low mismatch at γ/γ′ interface, and low anti-phase boundary energy (APBE) of the precipitates (Pineau and Antolovich 2009, Vorontsov et al. 2012). The APBE results from the ordered nature of the γ' phase when energetically unfavorable bonds are formed due to dislocation motion (Reed 2006). This property is measurable and has been shown to have an impact on the response of superalloys (Gong et al. 2016). Looping of dislocations around precipitates is favored by large γ′ particles, low volume fraction, high APBE, and high mismatch at γ/γ′ interface (Pollock and Argon 1992, Link et al. 2009, Francis et al. 2014).

Due to the stoichiometric order of the $L1_2$ phase, dislocations are unable to move through the γ′ precipitates unless they travel in pairs. The first dislocation entering a γ' forms an anti-phase boundary while the second $a/2\ \langle 1\bar{1}0\rangle\{111\}$ trailing dislocation removes it, hence providing a resistance for the material to deform (Reed and Rae 2014). Depending on the size of the γ′ precipitates and their spacing, the dislocation-precipitate interaction can be classified as either weak or strong. Force equilibrium of weakly and strongly coupled dislocations has shown that the right balance between volume fraction and precipitate size can promote hardening by increasing the critically resolved shear stresses on the precipitates (Nembach and Neite 1985). The γ' precipitates are metastable. If sufficient temperature and stress is applied, they evolve to coarsen and change morphology forming rafts that are oriented depending on the stress state and lattice misfit. Rafting can influence both the constitutive response and the fatigue and creep rupture life of the superalloys. Rafts formed under tension, oriented perpendicular to the loading axes in these negative misfit alloys, have been shown to accelerate the creep rate under non-isothermal conditions (Giraud et al. 2012), accelerate the onset of tertiary creep for isothermal creep (Nathal and Mackay 1987), and reduce the tensile strength at high temperatures (MacKay and Ebert 1985). Rafts formed under compression, oriented parallel to the compression axis, have been shown to improve isothermal fatigue strength (Tetzlaff and Mughrabi 2000) and tensile creep strength

(Shui et al. 2006), and to have little effect on creep for relatively low stresses (Nabarro 1996, Reed et al. 1999). Rafting has also been shown to reduce the thermomechanical fatigue life of specimens by up to a factor of 5 (Arrell 2004, Kirka 2014).

In second-generation rhenium and ruthenium containing superalloys, the creep rate response can be demarcated by the stress and temperature regimes, shown in Figure 1 (Pollock and Argon 1992, Reed 2006, Ma et al. 2008, Tinga et al. 2010). At low temperatures and high stresses, the deformation mechanism that dominates is that of shearing of the γ' particles by dislocations ribbons of overall Burgers vector $a\langle 11\bar{2}\rangle$ dissociated into superlattice partial dislocations separated by a stacking fault (Pollock and Argon 1992, Reed and Rae 2014). For instance, CMSX-4 exhibits primary creep when the uniaxial normal stress is greater than 550 MPa, this value will vary across different alloys but in general sufficient stress needs to be applied to shear the γ' precipitates and promote primary creep (Reed 2006). Primary creep is a process involving nucleation, propagation and termination of mobile $a\langle 11\bar{2}\rangle$ dislocation ribbons requiring sufficient densities of at least two $a/2\,\langle 1\bar{1}0\rangle\{111\}$ families of dislocations in the γ channels to enable the nucleation of the dislocations and sufficient resolved shear stress for the propagation of the $a\langle 11\bar{2}\rangle$ ribbon. At higher temperatures and lower stresses, primary creep is less prominent because dislocations cannot shear the precipitates and tertiary creep becomes more dominant. Although during tertiary creep at high temperature other slip systems can become active, such as the cubic slip systems, most of the dislocations are restricted to the octahedral slip systems in the γ channels (Bettge and Österle 1999). At the lower stress level during tertiary creep, the dislocations at the γ/γ' interface cannot push through the γ' precipitates due to the high energy associated with the anti-phase boundary (APB) in the γ' precipitates, and as a result the dislocations must loop around the them (MacKay and Ebert 1985, Matan et al. 1999). For second-generation superalloys, in the tertiary creep regime the dominant dislocation mechanism is $a/2\,\langle 1\bar{1}0\rangle\{111\}$ with these dislocations primarily

being screw in nature. Further, the deformation that occurs is homogeneous, generally with more than two slip systems active (Pollock and Argon 1992, Matan et al. 1999). Another explanation for the onset of tertiary creep is the topological inversion of the material phases, so that the γ′ becomes the matrix and an acceleration in the creep rate is seen a result of the ease in which $a\langle 100\rangle$ dislocations can move through the interconnecting γ' matrix (Epishin and Link 2004).

The deformation mechanisms that activate during cyclic loading are also dependent on temperature. At low temperatures, generally below 750 °C, the deformation is usually dominated by the γ′ precipitates shearing. The dislocation motion is heterogeneous and restricts itself to the $a/2\,\langle 1\bar{1}0\rangle\{111\}$ systems with limited cross-slip. However in the case of large plastic deformation the dislocation motion becomes more homogeneous thus decreasing the formation of the slip bands (Shyam and Milligan 2004). As the temperature increases a deformation-induced coarsening takes place leading to dislocation looping. Also, cross-slip is enhanced due to thermal activation making dislocations more mobile in the γ channels. Additionally, the dislocation activity becomes more homogeneous but a small number of slip bands can still be observed (Pineau and Antolovich 2009).

3. CRYSTAL VISCOPLASTICITY MODEL FOR MODELING CREEP-FATIGUE LOADING OF CMSX-8

The model proposed extends the crystal viscoplasticity formulation originally developed by Ma, Dye, and Reed (Ma et al. 2008) by adding the elements needed capture cyclic loading. A key feature of their model is the additive contribution of the material phases (γ and γ') to the deformation in the plastic velocity gradient. Traditionally when modeling superalloys, only one functional form of the shearing rates on all slip systems is assumed for the two phases in the unit cell which, when calibrated with macroscopic data, forcefully limits the model to give an average measure of deformation,

$$\mathbf{L}^{in} = \dot{\mathbf{F}}^{in}\,\mathbf{F}^{in^{-1}} = \sum_{\alpha=1}^{N_{slip}} \dot{\gamma}^{in(\alpha)} \left(\hat{\mathbf{d}}_o^{(\alpha)} \otimes \hat{\mathbf{n}}_o^{(\alpha)}\right) \tag{1}$$

where $\mathbf{L}^{in}$ is the inelastic velocity gradient, $\mathbf{F}^{in}$ is the inelastic deformation gradient, $\dot{\gamma}^{in(\alpha)}$ is the inelastic shearing rate on the α^{th} slip system, $\widehat{\boldsymbol{d}}_{\mathbf{0}}^{(\alpha)}$ and $\widehat{\boldsymbol{n}}_{\mathbf{0}}^{(\alpha)}$ are the slip direction and slip plane normal unit vectors respectively, defined in the reference configuration for each slip system, and N_{slip} is the number of possibly active slip systems. A more appropriate description of plastic deformation should consider the distinct deformation mechanisms of the two phases. In some literature, this concern has been addressed by meshing a microstructure unit cell with two distinct constitutive relations for the γ and γ' phases, then either dislocation dynamics or the traditional crystal-plasticity finite element method is used to connect the microstructure behavior to the macroscale through diverse homogenization techniques (Busso et al. 2000, Forest et al. 2000, Dumoulin et al. 2003, Kumar et al. 2006, Wang et al. 2006, Messerschmidt 2010, Tinga et al. 2010, Hafez Haghighat et al. 2013). A downside of this approach is that it does not allow for immediate application to macroscopic components.

A major assumption in the model proposed by Ma, Dye, and Reed (Ma et al. 2008) is that the contribution to the overall deformation of the γ and γ' phase can be additively separated in the plastic velocity gradient as,

$$\mathbf{L}^{in} = f_{\gamma}\left(\sum_{\alpha=1}^{12}\dot{\gamma}_{\gamma}^{in(\alpha)}\left(\hat{\mathbf{d}}^{(\alpha)}\otimes\hat{\mathbf{n}}^{(\alpha)}\right)\right)+ f_{\gamma'}\left(\sum_{\alpha=13}^{24}\dot{\gamma}_{L1_2}^{in(\alpha)}\left(\hat{\mathbf{d}}^{(\alpha)}\otimes\hat{\mathbf{n}}^{(\alpha)}\right)\right) \tag{2}$$

where f_{γ} and $f_{\gamma'}$ are the volume fractions of the γ and γ' phases respectively, and $\dot{\gamma}_{\gamma}^{in(\alpha)}$ and $\dot{\gamma}_{L1_2}^{in(\alpha)}$ are the inelastic shearing rates on the α^{th} slip systems of the γ and γ' phase, respectively. Deformation is assumed to occur on the *<111>* plane for both material phases. As illustrated in Figure 2, in the γ channels climb and glide of dislocations is considered while shearing of the precipitates through dislocation ribbons is considered in the γ' phase. Equation (2) admits distinctly different flow rules for both material phases and weights their contributions to the total deformation by their volume fraction.

Moreover, this additive decomposition is assumed over all material elements. Therefore, deformation on the γ and γ' phases can be modeled without having to mesh the basic microstructure unit. This offers a major advantage over traditional models because it allows for immediate application to macroscopic components since no additional homogenization steps are needed between the microstructure and the component level. In equation (2), the slip systems in the γ phase are assumed to be octahedral for all slip systems; i.e., $\hat{n}^{(\alpha)}||\{111\}$. In the γ' phase, the primary octahedral slip planes still operate, $\hat{d}^{(\alpha)}||\langle 111\rangle$, however dislocations cutting through γ' depend on the shear stress acting on partial dislocations necessary to cut through the ordered structure that manifests as ribbon shearing; hence, $\hat{d}^{(\alpha)}||\langle 112\rangle$ for $13 \leq \alpha \leq 24$.

3.1 INELASTIC SHEAR STRAIN RELATIONS AND EVOLUTION EQUATIONS

The relationship between the inelastic strain rates on each slip system and the velocity of mobile dislocations is assumed to follow modifications of the Orowan equation for both material phases (Orowan 1940). In the work of Ma et al. (Ma et al. 2008) the flow rule was limited to uniaxial creep because the effective stress did not include the effect of the backstress during load reversals. Furthermore, the strain rate sensitivity of the material was not considered which is necessary to model different loading rates during operation, i.e. the loading ramps versus strain or stress dwells. Additionally, the shearing rates were all assumed to be positive, which could only possibly be true for the case of simple uniaxial tensile loading. In this paper, the flow rule of Ma et al. has been extended to predict the more general case of 3-D creep-fatigue interactions. In the γ phase the following flow rule for each primary slip system is proposed:

$$\dot{\gamma}_{\gamma}^{in(\alpha)} = \rho_{\gamma}^{(\alpha)} b \lambda_{\gamma}^{(\alpha)} F_{attack} \Theta(T) \left(\frac{\tau_{eff_{\gamma}}^{(\alpha)}}{\kappa_{\gamma}^{(\alpha)}} \right)^{n} \exp\left(\frac{-Q_{slip}^{110} + \left(\left| \tau_{eff_{\gamma}}^{(\alpha)} \right| - \kappa_{\gamma}^{(\alpha)} \right) V_{c1}^{(\alpha)}}{kT} \right) sign\left(\tau_{eff_{\gamma}}^{(\alpha)} \right) \quad (3)$$

where $\dot{\gamma}_{\gamma}^{in(\alpha)}$ is the inelastic shearing rate in the γ phase in the α^{th} slip system, *b* is the magnitude of the burgers vector, $\lambda_{\gamma}^{(\alpha)}$is the mean obstacle spacing in the γ phase, F_{attack} is the dislocation vibration frequency, $\theta(T)$ is a diffusivity parameter, $\tau_{eff_{\gamma}}^{(\alpha)}$ is the effective resolved shear stress on the α^{th} slip system, $\kappa_{\gamma}^{(\alpha)}$is the threshold stress on the α^{th} slip system, Q_{slip}^{110} is the activation energy for slip on the γ phase, $V_{c1}^{(\alpha)}$is the activation volume in the α^{th} slip system, *T* is temperature and *k* is the Boltzmann's constant.

The diffusivity parameter is composition sensitive and is calibrated to the alloy's Re content using thermodynamics and kinetic software Thermo-Calc and DICTRA (Thermo-Calc Software, Solna, Sweden). The diffusivity parameter is assumed to be of the form,

$$\Theta(T) = C_1 \left(\frac{T}{T_{melt}} \right)^{C_2} \exp\left(-\frac{Q_o}{kT} \right) \tag{4}$$

where C_1 and C_2 are model parameters, T_{melt} is the melting temperature of the γ phase, and Q_0 is the effective activation energy for diffusion. The pre-exponential coefficient is calibrated using macroscopic creep test data while the activation energy for diffusion is composition sensitive and is calculated using Thermo-Calc and DICTRA following the procedure outlined by Gorgannejad et al. (Gorgannejad et al. 2016) and by Estrada Rodas et al. (Estrada Rodas et al. 2016).

To model load reversals during creep-fatigue loading, a sign function in the flow rule has been added which reverses the shearing rates in the direction of the applied loading. A power law term was also added to account for the strain rate sensitivity, and is needed to model different strain rates during creep-fatigue interactions. The activation energy Q_{slip}^{110} represents the thermal component for overcoming the obstacles in absence of stress. The exponential term in the flow rule describes the

probability of dislocations moving. The pre-exponential coefficient accounts for the speed of the mobile dislocations and is dependent on the mobile dislocation density on that slip system, the Burger's vector, the dislocation vibration frequency, and the dislocation mean free path which is defined as (Ma et al. 2008),

$$\lambda_{\gamma}^{(\alpha)} = c_{jump1}\left(\frac{1}{L_{\gamma}} + \frac{1}{L_{\rho}^{(\alpha)}}\right)^{-1} \tag{5}$$

where c_{jump1} is a model parameter, L_{γ} is the size of the γ channels, and $L_{\rho}^{(\alpha)}$ is the spacing of forest dislocations. The dislocation mean free path (jump distance) is an average measure of the distance travelled by dislocations between the source and storage points and is proportional to the dislocation pinning spacing. The components due to pinning at the γ/γ' interfaces and the average spacing of forest dislocations is assumed to be (Ma et al. 2008),

$$L_{\rho}^{(\alpha)} = \frac{c_{Fdis}}{\sqrt{\rho_{F}^{(\alpha)}}} \tag{6}$$

where c_{Fdis} is a model parameter, and $\rho_{F}^{(\alpha)}$ is the forest dislocation density. The effective resolved shear stress is considered as the contributions of the applied loading, the misfit stresses and the backstress:

$$\tau_{eff_{\gamma}}^{(\alpha)} = \tau_{\gamma}^{(\alpha)} + \tau_{mis}^{(\alpha)} - \chi_{\gamma}^{(\alpha)} \tag{7}$$

where $\tau_{\gamma}^{(\alpha)}$ is the resolved shear stress on the α^{th} slip system, $\tau_{mis}^{(\alpha)}$ is the misfit stress, and $\chi_{\gamma}^{(\alpha)}$ is the backstress. The backstress accounts for the Bauschinger effect which along with the sign function are important to model the reversibility of slip for creep-fatigue loading. The misfit stresses are assumed to relax due to the γ dislocations becoming captured in the γ/γ' interface which causes a loss of elastic coherency (Pollock and Argon 1992, Ma et al. 2008),

$$\tau_{mis}^{(\alpha)}\left(T,\gamma_{\gamma}^{(\alpha)}\right)=\tau_{mis0}^{(\alpha)}\left\{1-\exp\left(\left(\frac{\sum_{\alpha=1}^{12}\rho_{pb}^{(\alpha)}}{-\rho_{\gamma}^{ref}}\right)^{c_{icb}}\right)\right\} \tag{8}$$

where c_{icb} is a model parameter, and ρ_{γ}^{ref} is a model parameter representing the dislocation density for which the misfit stress completely relaxes. The threshold stress is assumed to rise from the hardening generated by the parallel dislocation density within the γ phase (Busso and McClintock 1996),

$$\kappa_{\gamma}^{(\alpha)}=\tau_{\gamma pass}^{(\alpha)}=c_{pass11}Gb\sqrt{\rho_{P}^{(\alpha)}} \tag{9}$$

where c_{pass11} is a model parameter, G is the shear modulus, and $\rho_{P}^{(\alpha)}$ is the parallel dislocation density. The forest and parallel dislocations characterize the resistance of mobile dislocations, these are defined by projecting the total dislocation density to the slip systems as (Ma and Roters 2004),

$$\rho_{F}^{(\alpha)}=\sum_{\beta=1}^{N_{slip}}\rho^{(\beta)}\left|\cos\left(\hat{\mathbf{n}}^{(\alpha)},\hat{\mathbf{n}}^{(\beta)}\times\hat{\mathbf{d}}^{(\beta)}\right)\right| \tag{10}$$

$$\rho_{P}^{(\alpha)}=\sum_{\beta=1}^{N_{slip}}\rho^{(\beta)}\left|\sin\left(\hat{\mathbf{n}}^{(\alpha)},\hat{\mathbf{n}}^{(\beta)}\times\hat{\mathbf{d}}^{(\beta)}\right)\right| \tag{11}$$

the activation volume is the volume that is physically swept by dislocations from a ground equilibrium state to an activated state after deformation (Ma et al. 2008, Sarkar and Chakravartty 2015),

$$V_{c1}^{(\alpha)}=c_{vc1}b^{2}\lambda_{\gamma}^{(\alpha)} \tag{12}$$

where c_{vc1} is a model parameter. In the γ' phase, the flow rule defines the rate of dislocation shearing through the γ' precipitates in a ribbon fashion on the secondary slip systems,

$$\dot{\gamma}_{L1_2}^{in(\alpha)}=\rho_{L1_2}^{(\alpha)}b\lambda_{L1_2}^{(\alpha)}F_{attack}\exp\left(\frac{-Q_{slip}^{112}+\left(\left|\tau_{eff_{\gamma'}}^{(\alpha)}\right|-\kappa_{L1_2}^{(\alpha)}\right)V_{c2}^{(\alpha)}}{kT}\right)sign\left(\tau_{eff_{\gamma'}}^{(\alpha)}\right) \tag{13}$$

where $\dot{\gamma}_{L1_2}^{in(\alpha)}$ is the inelastic shearing rate in the α^{th} slip system on the γ' phase, $\lambda_{L1_2}^{(\alpha)}$ is the mean obstacle spacing in the γ' phase, $\tau_{eff_{\gamma'}}^{(\alpha)}$ is the effective resolved shear stress on the α^{th} slip system in the γ' phase, $\kappa_{L1_2}^{(\alpha)}$ is the threshold stress on the α^{th} slip system in the γ' phase, and $V_{c2}^{(\alpha)}$ is the activation volume in the α^{th} slip system in the γ' phase.

In the γ' phase the dislocation mean free path (jump distance) is controlled by the size of the γ' particles $L_{\gamma'}$;

$$\lambda_{L1_2}^{(\alpha)} = c_{jump2}\left(\frac{1}{L_{\gamma'}} + \frac{1}{L_{\rho}^{(\alpha)}}\right)^{-1} \tag{14}$$

where c_{jump2} is a model parameter. In the model proposed by Ma et al., as dislocation density increased, the mean obstacle spacing approaches zero. This is undesirable because it artificially hardens the precipitates by creating infinite repelling forces between dislocations. A first order approximation of the minimum distance between two strongly-coupled dislocations entering a γ' precipitate was developed by Huther and Reppich (Huther and Reppich 1978) using force balance,

$$\lambda_{mim} = \frac{Gb^2}{2\pi\gamma_{APB}} \tag{15}$$

where γ_{APB} is the ABPE. Hence, in our model this distance has been assumed as the minimum value the mean obstacle spacing can reach. In the γ' precipitates the threshold stress has two components, the hardening generated by the passing of dislocations in this phase ($\tau_{L1_2 pass}^{(\alpha)}$) and the APB resistance created when a pair of dislocations enter the precipitate (τ_{APB}),

$$\kappa_{L1_2}^{(\alpha)} = \tau_{L1_2 pass}^{(\alpha)} + \tau_{APB} \tag{16}$$

unlike the model by Ma et al., the additional term in the passing stress in this phase, $\tau_{L1_2 pass}^{(\alpha)}$, accounts for the hardening associated with the increased incoherency at the γ/γ' interface induced by increased dislocation density at the interface;

$$\tau_{L1_2 pass}^{(\alpha)} = Gb\left(c_{pass21}\sqrt{\rho_P^{(\alpha)}} + c_{pass22}\sqrt{\rho_{P_{pb}}^{(\alpha)}} \right) \tag{17}$$

where c_{pass21} and c_{pass22} are model parameters, and $\rho_{P_{pb}}^{(\alpha)}$ is the parallel dislocation density at the γ/γ' phase boundary. The APB resistance is described by the APBE as (Reed 2006),

$$\tau_{APB} = \frac{\gamma_{APB}}{b} \tag{18}$$

the effective stress in the precipitates is comprised of the applied stress resolved onto the secondary slip systems:

$$\tau_{eff_{\gamma'}}^{(\alpha)} = \tau_{\gamma'}^{(\alpha)} \tag{19}$$

where $\tau_{\gamma'}^{(\alpha)}$ is the resolved shear stress on the α^{th} slip system in the γ' phase. After reaching the critical stress level for precipitate shearing, the precipitate offers very little resistance to dislocation motion and therefore the backstress is not included in the γ' phase. Moreover, the effect of the misfit stress is strongest at the γ/γ' interface and before shearing has taken place, therefore it is only accounted for in the γ phase.

In the model by Ma et al. (Ma et al. 2008), the evolution of dislocation densities in the γ phase and in the γ' phase were both considered. However, the evolution of dislocations at the γ/γ' phase boundary also is important to track. The process of shearing of the precipitates starts with an initial

population of dislocations in the γ channels which evolves, climbs and glides to later populate the γ/γ' interphase. Enough dislocations need to form at this interphase before shearing of the γ' precipitates can occur. Therefore, the dislocation density at the γ/γ' phase boundary also needs to be an ISV. Hence, the dislocation density in the γ channels, in the γ' particles and in the γ/γ' interface will be controlled by unique sets of evolution equations since their values are often distinctly different, particularly under conditions when looping of the precipitates occurs. In the γ channels, the dislocation density assumes a Kocks-Mecking form (Kocks and Mecking 2003),

$$\dot{\rho}_{\gamma}^{(\alpha)} = \frac{c_{mult1}}{b\lambda_{\gamma}^{(\alpha)}}\left|\dot{\gamma}_{\gamma}^{in(\alpha)}\right| - c_{annh1}\rho_{\gamma}^{(\alpha)}\left|\dot{\gamma}_{\gamma}^{in(\alpha)}\right| \tag{20}$$

where c_{mult1} and c_{annh1} are model constants. This equation assumes that the evolution just depends on self-hardening and can be easily extended if needed to include cross-hardening. The evolution equations for dislocations gathered at the interface also uses the Kocks-Mecking form and are dependent on the shearing rates in the γ channels:

$$\dot{\rho}_{pb}^{(\alpha)} = \frac{c_{mult}^{pb}}{bL_{\gamma}}\left|\dot{\gamma}_{\gamma}^{in(\alpha)}\right| - c_{annh}^{pb}\rho_{pb}^{(\alpha)}\left|\dot{\gamma}_{\gamma}^{in(\alpha)}\right| \tag{21}$$

where c_{mult}^{pb} and c_{annh}^{pb} are model parameters, and $\rho_{pb}^{(\alpha)}$ is the dislocation density in the γ/γ' phase boundary in the α^{th} slip system. In the γ' particles, the evolution equations include one more multiplication term that captures the ease of a dislocations entering the γ' particle, and is controlled by a thermally activated process (Ma et al. 2008),

$$\dot{\rho}_{L1_2}^{(\alpha)} = c_{mult21}\rho_{pb}^{(\alpha)}\Gamma + \frac{c_{mult22}}{b\lambda_{\gamma'}^{(\alpha)}}\left|\dot{\gamma}_{\gamma'}^{(\alpha)}\right| - c_{annh2}\rho_{\gamma'}^{(\alpha)}\left|\dot{\gamma}_{\gamma'}^{(\alpha)}\right| \tag{22}$$

where c_{mult21}, c_{mult22}, and c_{annh2} are model parameters, $\rho_{pb}^{(\alpha)}$ is the dislocation density in the γ/γ' phase boundary, and Γ is a thermally activated function describing the process of dislocations forming at the phase boundary and then becoming able to shear the precipitates,

$$\begin{cases} \Gamma = F_{attack} \exp\left(\dfrac{-Q^{pb} + \left(\left| \tau^{(\alpha)} \right| - \tau_{pb_{pass}}^{(\alpha)} \right) V_{c2}^{(\alpha)}}{kT} \right) sign\left(\left| \tau^{(\alpha)} \right| - \tau_{pb_{pass}}^{(\alpha)} \right) \\ Q^{pb} = c_{misfit} G b^3 \left| \delta \right| \\ \tau_{pb_{pass}}^{(\alpha)} = c_{pass}^{pb} G b \sqrt{\rho_{P_{pb}}^{(\alpha)}} \end{cases} \tag{23}$$

where c_{misfit} and c_{pass}^{pb} are model parameters, and δ is the lattice misfit. This additional multiplication term in equation (22) considers the contribution from the dislocations that are generated in the channels and then gather at the phase boundary (γ/γ' interface). When enough dislocations gather at the interface and when enough stress is provided, they can start cutting the precipitates. Also, unlike the model proposed by Ma et al. (Ma et al. 2008), an increase in $\rho_{L1_2}^{(\alpha)}$ does not lead to additional hardening because the threshold stresses in the γ and γ phase do not depend on $\rho_{L1_2}^{(\alpha)}$ or on $\gamma_{L1_2}^{(\alpha)}$. The hardening in the precipitates is mostly due to the APBE but it also has contributions from dislocation networks that form at the γ/γ' interface. In our model, only the shearing rates, $\dot{\gamma}_{L1_2}^{(\alpha)}$, are directly proportional to $\rho_{L1_2}^{(\alpha)}$, hence after dislocations have sheared the precipitates, the precipitates do not become hardened by multiplication of dislocations inside them. This better describes the process of the movement of dislocations from the γ channels to the γ' precipitates and through them.

The evolution of the backstress has the form (Shenoy et al. 2008),

$$\dot{\chi}_{\gamma}^{(\alpha)} = C_{\chi}\left\{\eta C_{44} b\sqrt{\rho_{\gamma}^{(\alpha)}}\,\mathrm{sgn}\left(\tau_{\gamma}^{(\alpha)} - \chi_{\gamma}^{(\alpha)}\right) - \chi_{\gamma}^{(\alpha)}\right\}\left|\dot{\gamma}_{\gamma}^{(\alpha)}\right| \tag{24}$$

$$\eta = \frac{\eta_o \dfrac{c_{mult1}}{b\lambda_{\gamma}^{(\alpha)}}}{\dfrac{c_{mult1}}{b\lambda_{\gamma}^{(\alpha)}} + \kappa\sqrt{\rho_{\gamma}^{(\alpha)}}} \tag{25}$$

the backstress is used to capture the Bauschinger effect associated with the resistance of dislocation glide in the matrix. This formulations assumes that the backstress also captures the contribution of the Orowan stress, which relates to the bowing of the dislocations in the γ channels between the precipitate interfaces and is dependent on the dislocation mean free path and therefore is a function of dislocation density in the channels (Busso and McClintock 1996).

3.3. PARAMETER ESTIMATION AND MODEL VERIFICATION

The objective in determining the material parameters was to reproduce the stabilized cyclic response for the purposes of using the response to predict LCF and TMF crack formation life (Zamrik and Renauld 2000, Vose et al. 2013, Kulawinski et al. 2015). Hence, the transient evolution of the γ and γ' phases that occurs during the first few cycles, particularly in the cases of strain or stress holds and before the stabilized condition is reached, was not used to calibrate the parameters. Therefore, the influence of this microstructure evolution is implicitly captured through the material parameters. To explicitly include this influence, it would be necessary to have a kinetic model of this shorter-term transient behavior, which unfortunately is not available presently. The ASTM E2714-13 standard for isothermal creep-fatigue testing was followed to generate hysteresis data to fit the model parameters. The tests were performed on single-crystal Ni-base superalloy CMSX-8[B/C] in the <001> and in the <111> orientation. The nominal composition of superalloys commonly used in the hot-gas path, including that of CMSX-8, are listed in Table 1. The creep-fatigue experiments were conducted under strain control at

a strain rate of $1x10^{-3}$ (1/s) for strain ratios of $-\infty$ and 0. These ratios were used because they are more representative of turbine operating conditions since there are regions in turbine blades that only experience negative loads while others only experience positive ones. The creep relaxation holds were of 3 minutes applied at the absolute maximum strain magnitude. The temperatures tested ranged from 750°C to 1100°C. This temperature range was selected so that the deformation mechanisms attributed to one or both phases were present. This is important since shearing of the precipitates is dominant at lower temperature and at higher stresses, while glide and climb is dominant at higher temperatures which will allow calibration of each term in the flow rule.

Presently, a test program on CMSX-8 is in progress to determine the constitutive response dependence on the rafted state at Georgia Tech. Essentially, the procedure outlined and used by Epishin et al. (Epishin et al. 2008) for CMSX-4 is being used to generate rafted CMSX-8 microstructures by subjecting virgin test specimens that had been heat-treated to the standard blade treatment to a constant stress and constant temperature over a prolonged period of time to generate a prescribed coarsened and raft condition. These exposed specimens will then be fatigue-cycled with the same conditions used on the virgin specimens at different temperatures. Early results (Gorgannejad and Neu 2017) suggest that the initial transient stress-strain response is different between the rafted and virgin microstructures as might be expected, but the stabilized macroscopic cyclic constitutive response after the initial transient cycles for most of the creep-fatigue cycles relevant to IGT applications is nearly independent of the initial microstructure. Yet, the fatigue life of the specimens does still depend on the raft state similar to what has been reported by others (Ott and Mughrabi 1999). Despite not modeling the rafting and not meshing the basic microstructure unit, equation (2) can include several relevant aspects of the microstructure. First, the volume fraction serves as a weight reflecting the phase contributing the most to the overall deformation. Second, the Schmidt tensors for each phase are

distinct. Third, and perhaps more importantly, separating the plastic velocity gradient for the material phases also allows for explicitly incorporating two distinct flow rules and distinct evolution equations for the dislocation densities for each material phase which more closely resembles the deformation mechanisms in superalloys. Next, we describe in detail the proposed flow rules for the γ and γ' phase.

The equilibrium volume fraction of γ' precipitates depends on temperature and with sustained exposure to high temperatures it can be reduced; for example, a superalloy with 70% γ' at room temperature could experience a reduction to 45% γ' with sustained exposure to 1100°C (Yandt et al. 2012). Since it is impractical to measure the volume fraction of the precipitates as a function of temperature and exposure time, the room temperature volume fraction was used as nominal value for purposes of decomposing the deformation in the two phases. While one could potentially in the future evolve this volume fraction with temperature and time, in our calibration exercise, because the main interest was to predict the stabilized cyclic response, the volume fraction was fixed at the room temperature value and the channel size was fixed to 0.1 μm. The physical parameters used in this model are shown in Table 2, these are parameters that can often be calculated by first principles or are known via independent experiments (Pyczak et al. 2004, Reed 2006, Ma et al. 2008, Yandt et al. 2012, Daniel Leidermark 2016, Gong et al. 2016). The remaining material parameters are shown in Table 3 and are determined by calibrating the model to creep-fatigue data at 1100°C and at 750°C, while leaving the intermediary temperatures as verification sets. The data at 1100°C is used to calibrate the parameters for the γ phase while the data at 750°C is used to calibrate material parameters associated to the γ' phase. The resulting calibrated parameters are presented in Table 3. While the model is sensitive to all parameters, a subset of these parameters tends to affect the constitutive response to a greater amount. These are noted in bold in Table 3. Changes in these parameters were used during the coarse calibration, while fine tuning was achieved by adjusting the remaining parameters. The thermoelastic

parameters are functions of temperature and are calibrated from experimentally obtained moduli, yield strength, and elastic thermal strain data shown in Figure 3. However, none of the viscoplastic parameters in Table 2 and Table 3 depend directly on temperature. Temperature dependence is accounted for in in the strain rate relationships (equations (3) and (13)) and through the diffusivity parameter (equation (4)). To model TMF loading, the procedure outlined by Shenoy et al. (2006) is used and the thermoelastic properties and the model parameters are held constant at their values at the beginning of the time step. This approach is reasonable for small time steps. The implementation of the finite element UMAT uses the standard multiplicative rule for the deformation gradient that includes the rigid rotation of the crystal lattice (Bilby et al. 1955, Sheh and Stouffer 1988, Srikanth and Zabaras 1999). Due to its numerical stability for implementing crystal plasticity, a modified Newton-Raphson method is used to solve the values of the flow rules at each time step (McGuinty 2001). Because in the model the plastic velocity gradient has two flow rule summations, the complexity of the implementation of the Newton-Raphson method is significantly increased. This implementation is not trivial and is addressed in detail elsewhere (Estrada Rodas 2017). As is shown in Figure 4, the calibrated parameters used in this model result in simulations that are in good agreement with the experimental data. Note that the model not only readily estimates the stabilized hysteresis but also provides good estimations of important features in the deformation such as the yield strength, amount of stress relaxation and amount of cyclic creep.

4. MODEL VALIDATION AND DISCUSSION

4.2 MODEL VALIDATION

The model was exercised to validate its application outside of the creep-fatigue conditions that were used to calibrate it. A creep-fatigue experiment was performed at a very large strain range outside of the range used during the calibration. The test was conducted at 750°C with 20 minute holds both at maximum tension and compression with a strain range of 2%, a strain rate of $1x10^{-3}$ (1/s), and strain

ratio (*R*) of -1. In Figure 5, we plot the experimental and simulated hysteresis. It is interesting to observe that the model correctly predicts the rather surprising amount of stress relaxation that would take place at 750°C under these loading conditions. Furthermore, isothermal fatigue and thermomechanical fatigue (TMF) experiments, are shown in Figure 6 along with the predictions by the model. The differences between the predictions and the experimental results at 750°C are attributed to the experimental variance of the moduli. The differences between the predictions and the experimental results in the TMF cycle could be attributed to not modeling the evolution of the microstructure. However, note that this model is able to predict the cyclic creep that takes place during the first few cycles of TMF and lack of thereof during the first few cycles of the isothermal fatigue at lower temperatures.

4.3 SENSITIVITY STUDY

The model includes several parameters that are relevant to the microstructure, for instance the volume fraction of the phases, size of the precipitates and the value of the APBE. A clear advantage of including these in the modeling is that the effect of changes on microstructural features can be explored which can provide insightful direction when designing alloys. In this section, a sensitivity study is performed on the APBE, the γ channel size and the initial value of dislocation densities in the channels. The sensitivity studies are done at high temperatures where the γ phase dominates the deformation and at lower temperatures where the γ' phase dominates. Isothermal creep-fatigue tests were simulated at 1100°C and at 750°C. Periods of 3-minute holds were used for the higher temperature and of 20 minutes for the lower temperature so as to allow comparisons with the experimental results reported in this work. All the simulations used a strain rate of $1x10^{-3}$ (1/s) during the loading ramps.

In Figure 7, the sensitivity of the response to changes in the APBE is plotted. The model shows that increasing the APBE has a greater effect at the lower temperatures as shown in Figure 7. This is no

surprise considering that at these low temperatures and at these high stress level it is the γ' phase that provides the greatest resistance to the movement of dislocations. Reducing the APBE allows for more dislocations to cut through the precipitates. At higher temperatures, changes in the APBE affect the initial yield more than they affect the stabilized response. This could be attributed to the fact that precipitate shearing takes place during initial loading due to the higher stresses. As cycling is continued, the dislocations begin to stabilize and the material hardens which reduces the effective stress seen by the precipitates.

Another important microstructure feature in the superalloys is the γ channel size and volume fraction of γ'. Superalloys have been developed for many decades and currently there exists my types and generations of superalloys with various volume fraction of γ and γ'. It has been shown in multiple studies that there is a direct correlation between γ' particle size and hardening, and that the optimum strength in superalloys takes place at the transition from weak to strong coupling (Reppich 1982, Reppich et al. 1982). In Figure 8, the γ channel size has been increased while keeping the volume fraction of γ' precipitate constant and while varying the size of the precipitates according to the constraint (Ma et al. 2008):

$$f_{\gamma'} = \frac{L_{\gamma'}^3}{\left(L_\gamma + L_{\gamma'}\right)^3} \tag{26}$$

This analysis shows that increasing the channel size reduces the yield strength, reduces the hardening rate, and reduces the flow stress during the initial loading; while in subsequent loading increases the plastic strain range and the amount of stress relaxation of the stabilized hysteresis.

Finally, the initial amount of dislocations in the γ channels is representative of different aging

heat treatments (Pollock and Argon 1992, Wilson and Fuchs 2008). In Figure 9, the dislocation densities are varied by two orders of magnitude, this variation shows that increasing the initial dislocation density increases the initial strength of the material however little effect is seen in the stabilized hysteresis of the alloys.

4.4 CASE STUDY: INSIGHTS INTO STRENGTHENING BEHAVIOR OF SUPERALLOY SINGLE-CRYSTALS

The model can be used to further the understanding of the mechanical behavior of superalloys. In a recent study into the strengthening mechanisms of single-crystal superalloys (le Graverend et al. 2016), specimens were heated to 1050°C, subsequently a rapid thermal jump to 1200°C was performed at a heating rate of 30 (°C/s). These jumps were allowed to stabilize at 1200°C for periods of 30 seconds or 150 seconds while holding zero force. Then the specimens were rapidly cooled down to 1050°C at 30 (°C/s) and loaded monotonically. In the study, the authors compared the effect of the 30 second jump duration and the 150 second one to specimens with no thermal jumps. Under these conditions le Graverend et al. found a transient increase in strength of 160MPa for both thermal jump conditions with respect to the as-heat-treated condition. In the study, it was argued that this transient increase was due to the precipitation of fine γ' particles which pinned dislocations in the channels. It was furthered theorized that after the dissolution of these particles the alloy lost its transient increase in strength. In Figure 10, we plot the changes in the mechanical response when c_{jump1} is increased and decreased from its current value of 0.09 by 0.01. In this simulation, the same loading conditions used by le Graverend et al. were applied. It was decided to vary c_{jump1} because in the model this viscoplastic parameter is directly proportional to the mean obstacle spacing. This provides a first order approximation to the experimental observations made by le Graverend et al., if fine γ' prime obstacles were present in the channels then c_{jump1} would be reduced. From Figure 10 it can be seen that the model predicts increased strength for the simulation with lower c_{jump1} and decreased strength for the simulation with higher one.

These simulations show that the effect of obstacle spacing in strength is most pronounced during the initial loading; after the change in strain rates, the effect appears to vanish. Hence, the model suggests that it is indeed possible that the transient hardening observed in the experiments of le Graverend et al. is due to the formation of pinned dislocations at finer γ' particles. It is worth noting that the model has not been calibrated to the material used by le Graverend et al. and therefore the comparisons on this study are only qualitative. Moreover, the rather simplistic approach that we have proposed would need to be refined if greater level of fidelity was necessary. However, this example serves to show the capability of the model to help alloy and component designers understand the mechanical behavior of the superalloys and propose better designs.

4.5 MODEL LIMITATIONS

The model has shown that it can capture the mechanical behavior of superalloys over a very wide range of temperature regimes. However, a universal set of parameters that worked for all temperatures in the *<001>*, and in the *<111>* orientation could not be established. In the modeling work of Ma et al. (Ma et al. 2008) the authors did not directly compared their simulations to CMSX-4 specimens in the <111> orientation and only the trend of the deformation in different orientations was reported. Ma et al. compared their uniaxial creep simulations to experimental results by MacKay and Meier (MacKay and Maier 1982) and found that their model incorrectly predicted the softest orientations to be between the *<101>* and the *<111>* crystallographic orientation. Ma et al. argued that, since their model was not implemented as a 3-D finite element code, the discrepancy was due to the 1-D routine not being able to account for the change in crystal orientation during loading. In our formulations, the lattice rotation has been included, still the model experiences the same shortcoming. To diagnose the problem, the material parameters were varied until reaching better correlation with the <111> results. This exercise helps determine terms in the current formulation of the model that need modifications to account for the effect of orientation. It was found that the dislocation mean obstacle spacing ($\lambda_\gamma^{(\alpha)}$), and the

threshold stress ($\kappa_{L1_2}^{(\alpha)}$) need further development to properly model the effect of crystallographic orientation.

To better approximate the <111> results, parameter c_{jump1} in $\lambda_{\gamma}^{(\alpha)}$ was increased from 9x10^{-2} to 0.3, and γ_{APB} was decreased from 0.111(J/m^2) to 0.02 (J/m^2), as seen in Figure 11. This implies that the rather simplistic formulations assumed for the anti-phase boundary resistance and for the mean obstacle spacing are not enough to model other material orientations. These approximations are too crude to accurately reflect the geometric rotation of the microstructure from the $<001>$ to the $<111>$ orientation. Another possibility for the discrepancy between the simulations and the experimental data is the activation of cube slip which could act at high homologous temperatures. In the modeling it has been assumed that only the $\langle 110\rangle\{111\}$ slip systems are active, however it is possible that the six cube slip systems $\langle 100\rangle\{110\}$ activate due to their significantly higher resolved shear stress in the <111> orientation. Cube slip has been observed in superalloys at high temperatures and in orientations close to the <111> (Sun and Hazzledine 1996). Unfortunately, the role of cube slip on the deformation is still not well understood, but there is sufficient experimental data supporting possible activation of cube slip at high temperatures on both material phases (Österle et al. 2000, Daymond et al. 2007, Tinga et al. 2010, Weber and Ghosh 2016). Another aspect to note is that in contrast with the *<001>* orientation, in the *<111>* orientation a greater amount of plastic strain is present in the hysteresis when same strain amplitude is applied. This is due to larger elastic modulus in the *<111>* —2.6 times larger than in the *<001>* orientation at 1100°C. Consequently, the alloy yields at lesser strain in comparison with the *<001>* orientation. Also, after the first creep hold in the experimental data shown in Figure 11, the modulus of the *<111>* sample decreases by 17 GPa. Due to the large inelastic strain experienced by the sample, it is possible that it accumulated damage during the initial loading and during the creep hold which influenced the mechanical response. This suggests that additional modeling of damage is needed to

simulate the mechanical response of stiff orientations that can experience severe levels of plasticity at low applied strains. Additional CMSX-8 specimens in different orientations, other than the <001> and the <111>, were not available and hence no further insights or observations could be made to propose changes to the equations. However, the model without any changes still provides the correct trend of deformation. The influence of orientation on the mechanical response is plotted in Figure 12. In Figure *13* the mechanical responses for creep-fatigue tests in the $<001>$ and in the $<111>$ orientation are captured using the calibration obtained solely from experiments in the $<001>$ orientation. The model predicts a stiffer elastic response in the <111> and a larger plastic strain range in the stabilized hysteresis which is the correct trend.

5. SUMARY AND CONCLUSION

A Crystal Viscoplasticity (CVP) model for the creep-fatigue interactions targeting a second-generation single-crystal Ni-base superalloy CMSX-8 was proposed. The model is able to predict the deformation response under creep-fatigue and thermomechanical fatigue. In the CVP model the micromechanical deformation mechanisms of the γ channels and the γ' precipitate phases are explicitly considered and important attributes of the microstructure have been included. In previous modeling work by Ma et al. (Ma et al. 2008) two different flow rules were introduced in the velocity gradient which better resembles the deformation of Ni-base superalloy single-crystals. However, this model was limited to uniaxial stress-based creep. This work extended the Ma et al. (2008) model by 3-D creep-fatigue interactions by adding (1) a backstress and its evolution to provide for kinematic hardening to account for the Bauschinger effect during load reversals, (2) a strain rate sensitivity exponent to model changes in strain rate during cyclic loading excursions, and (3) the evolution of dislocations at the γ/γ' phase boundary is included to better model the process of dislocations forming in the γ channels and then piling-up at the interface before shearing the γ' precipitates. The model is implemented as an Abaqus User Material Subroutine (UMAT). Trade-off studies showed that the model correctly predicts known

trends of the deformation of second-generation Ni-base superalloys. Specifically, the sensitivity studies suggest that small variations in γ channel size can have a significant effect in the plastic behavior, with larger channel size leading to larger plastic strain range in the hysteresis loops, and lower yield strength. Implementing the model in its full 3-D, displacement-based formulation as an ABAQUS UMAT shows promise in exploring the effect of changes in critical microstructure parameters on the creep-fatigue response. This increased fidelity proposed in this model and its implementation in ABAQUS is a necessary first step that can allow designers construct sets of virtual experiments and that could help during alloy-process design and component performance. With further development, the model could be used to quantitatively assess the changes on the creep-fatigue response due to changes in the morphology of the γ' phase, hence serving as a structure-property tool for Integrated Computational Materials Engineering (ICME) of superalloys.

6. ACKNOWLEDGEMENT

This work was supported by U.S. Department of Energy, National Energy Technology Laboratory, University Turbine Systems Research (UTSR) Program, Grant DE-FE0011722, and Siemens Energy Inc., Orlando, FL.

Government or any agency thereof. The views and opinions of authors expressed herein do not necessarily state or reflect those of the United States Government or any agency thereof."

7. REFERENCES

Antolovich, S. D. (2015). "Microstructural aspects of fatigue in Ni-base superalloys." Philosophical Transactions of the Royal Society A: Mathematical, Physical and Engineering Sciences **373**(2038).

Arrell, D., Hasselqvist, M., Sommer, C., and Moverare, J. (2004). "On TMF Damage, Degradation Effects, and the Associated Tmin Influence on TMF Test Results in gamma/gamma prime Alloys." Superalloys 2004.

Bettge, D. and W. Österle (1999). ""Cube slip" in near-[111] oriented specimens of a single-crystal nickel-base superalloy." Scripta Materialia **40**(4): 389-395.

Bilby, B. A., R. Bullough and E. Smith (1955). "Continuous Distributions of Dislocations: A New Application of the Methods of Non-Riemannian Geometry." Proceedings of the Royal Society A: Mathematical, Physical and Engineering Sciences **231**(1185): 263-273.

Busso, E. P. and F. A. McClintock (1996). "A dislocation mechanics-based crystallographic model of a B2-type intermetallic alloy." International Journal of Plasticity **12**(1): 1-28.

Busso, E. P., F. T. Meissonnier and N. P. O'Dowd (2000). "Gradient-dependent deformation of two-phase single crystals." Journal of the Mechanics and Physics of Solids **48**(11): 2333-2361.

Cetel, A. D. and D. N. Duhl (1988). Second-generation nickel-base single crystal superalloy. Superalloys 1988. D. N. D. S. Reichman, G. Maurer, S. Antolovich, C. Lund. Pennsylvania, USA, The metallurgical society.

Cormier, J. and G. Cailletaud (2010). "Constitutive modeling of the creep behavior of single crystal superalloys under non-isothermal conditions inducing phase transformations." Materials Science and Engineering: A **527**(23): 6300-6312.

Daniel Leidermark, J. M. (2016). Comparative Analysis of Stress Relaxation and Creep in a Single-Crystal Superalloy. Proceedings of ASME Turbo Expo 2016: Turbine Technical Conference and Exposition, Seoul, South Korea.

Daymond, M. R., M. Preuss and B. Clausen (2007). "Evidence of variation in slip mode in a polycrystalline nickel-base superalloy with change in temperature from neutron diffraction strain measurements." Acta Materialia **55**(9): 3089-3102.

Dumoulin, S., E. P. Busso, N. P. O'Dowd and D. Allen (2003). "A multiscale approach for coupled phenomena in fcc materials at high temperatures." Philosophical Magazine **83**(31-34): 3895-3916.

Epishin, A. and T. Link (2004). "Mechanisms of High Temperature Creep of Nickel-base Superalloys under Low Applied Stress." Superalloys 2004: 137-143.

Epishin, A., T. Link, H. Klingelhoffer, B. Fedelich and P. Portella (2010). "Creep damage of single-crystal nickel base superalloys: mechanisms and effect on low cycle fatigue." Materials at High Temperatures **27**(1): 53-59.

Epishin, A., T. Link, M. Nazmy, M. Staubli, H. Klingelhöffer and G. Nolze (2008). "Microstructural Degradation of CMSX-4: Kinetics and Effect on Mechanical Properties." Superalloys 2008: 725-731.

Estrada Rodas, E. A. (2017). Microstructure-Sensitive Creep-Fatigue Interaction Crystal-Viscoplasticity Model for Single-Crystal Nickel-Base Superalloys. Ph.D., Georgia Institute of Technology.

Estrada Rodas, E. A., S. Gorgannejad, R. W. Neu, Z. Dyer, P. M. Draa, S.R. Shinde (2016). On the Development of ICME Tools for Creep and Aging of CMSX®-8. Superalloys 2016, John Wiley & Sons, Inc.**:** 665-674.
Fedelich, B., A. Epishin, T. Link, H. Klingelhöffer, G. Künecke and P. D. Portella (2012). Rafting during High Temperature Deformation in a Single Crystal Superalloy: Experiments and Modeling. Superalloys 2012, John Wiley & Sons, Inc.**:** 491-500.
Forest, S., F. Barbe and G. Cailletaud (2000). "Cosserat modelling of size effects in the mechanical behaviour of polycrystals and multi-phase materials." International Journal of Solids and Structures **37**(46–47): 7105-7126.
Francis, E. M., B. M. B. Grant, J. Q. d. Fonseca, P. J. Phillips, M. J. Mills, M. R. Daymond and M. Preuss (2014). "High-temperature deformation mechanisms in a polycrystalline nickel-base superalloy studied by neutron diffraction and electron microscopy." Acta Materialia **74**: 18-29.
Giraud, R., J. Cormier, Z. Hervier, D. Bertheau, K. Harris, J. Wahl, X. Milhet, J. Mendez and A. Organista (2012). "Effect of the Prior Microstructure Degradation on the High Temperature/Low Stress Non-Isothermal Creep Behavior of CMSX-4® Ni-Base Single Crystal Superalloy." Superalloys 2012: 265-274.
Gong, J., H. Z. D. A. Peralta, D. Snyder, M. P. Enright, J. McFarland, J. Neumann, J. Sebastian and G. Olson (2016). Integrated Thermal Process Optimization of Alloy 718PLUS® for Additive Manufacturing. Superalloys 2016. M. Hardy, E. Huron, U. Glatzel et al. Seven Springs, PA, TMS (The Minerals, Metals & Materials Society)**:** 1031-1040.
Gorgannejad, S., E. A. Estrada Rodas and R. W. Neu (2016). "Ageing kinetics of Ni-base superalloys." Materials at High Temperatures **33**(4-5): 291-300.
Gorgannejad, S. and R. W. Neu (2017). Unpublished results.
Gurrappa, I. and A. S. Rao (2006). "Thermal barrier coatings for enhanced efficiency of gas turbine engines." Surface & Coatings Technology **201**(6): 3016-3029.
Hafez Haghighat, S. M., G. Eggeler and D. Raabe (2013). "Effect of climb on dislocation mechanisms and creep rates in γ′-strengthened Ni base superalloy single crystals: A discrete dislocation dynamics study." Acta Materialia **61**(10): 3709-3723.
Harris, K., G. L. Erickson, S. L. Sikkenga, W. D. Brentnall, J. M. Aurrecoechea and K. G. Kubarych (1992). Development of the rhenium containing superalloys CMSX-4 and CM 186 LC for single crystal blade and directionally solidified vane applications in advanced turbine engines. Superalloys 1992. R. W. S. S. D. Antolovich, R. A. MacKay, D. L. Anton, T. Khan, R. D. Kissinger, D. L. Klarstrom. Warrendale, PA, The Minerals, Metals and Materials Society (TMS)**:** 297-306.
Huther, W. and B. Reppich (1978). "Interaction of Dislocations with Coherent, Stress-Free, Ordered Particles." Zeitschrift Fur Metallkunde **69**(10): 628-634.
Kirka, M. (2014). Thermomechanical behavior of a directionally solidified nickel-base superalloy in the aged state. Ph.D., Georgia Institute of Technology.
Kocks, U. F. and H. Mecking (2003). "Physics and phenomenology of strain hardening: the FCC case." Progress in Materials Science **48**(3): 171-273.
Kontis, P., D. M. Collins, S. Johansson, A. J. Wilkinson, J. J. Moverare and R. C. Reed (2016). Crack Initiation and Propagation During Thermal-Mechanical Fatigue of IN792: Effects of Dwell Time. Superalloys 2016, John Wiley & Sons, Inc.**:** 763-772.
Kulawinski, D., A. Weidner, S. Henkel and H. Biermann (2015). "Isothermal and thermo-mechanical fatigue behavior of the nickel base superalloy Waspaloy™ under uniaxial and biaxial-planar loading." International Journal of Fatigue **81**: 21-36.
Kumar, R. S., A.-J. Wang and D. L. Mcdowell (2006). "Effects of Microstructure Variability on Intrinsic Fatigue Resistance of Nickel-base Superalloys – A Computational Micromechanics Approach." International Journal of Fracture **137**(1): 173-210.

le Graverend, J.-B., J. Cormier, F. Gallerneau, S. Kruch and J. Mendez (2016). "Strengthening behavior in non-isothermal monotonic and cyclic loading in a Ni-based single crystal superalloy." International Journal of Fatigue **91, Part 1**: 257-263.
le Graverend, J. B., J. Cormier, F. Gallerneau, P. Villechaise, S. Kruch and J. Mendez (2014). "A microstructure-sensitive constitutive modeling of the inelastic behavior of single crystal nickel-based superalloys at very high temperature." International Journal of Plasticity **59**: 55-83.
Link, T., A. Epishin and B. Fedelich (2009). "Inhomogeneity of misfit stresses in nickel-base superalloys: Effect on propagation of matrix dislocation loops." Philosophical Magazine **89**(13): 1141-1159.
Ma, A., D. Dye and R. C. Reed (2008). "A model for the creep deformation behaviour of single-crystal superalloy CMSX-4." Acta Materialia **56**(8): 1657-1670.
Ma, A. and F. Roters (2004). "A constitutive model for fcc single crystals based on dislocation densities and its application to uniaxial compression of aluminium single crystals." Acta Materialia **52**(12): 3603-3612.
MacKay, R. A. and L. Ebert (1985). "The development of γ-γ′ lamellar structures in a nickel-base superalloy during elevated temperature mechanical testing." Metallurgical Transactions A **16**(11): 1969-1982.
MacKay, R. A. and R. D. Maier (1982). "The influence of orientation on the stress rupture properties of nickel-base superalloy single crystals." Metallurgical Transactions A **13**(10): 1747-1754.
Matan, N., D. C. Cox, P. Carter, M. A. Rist, C. M. F. Rae and R. C. Reed (1999). "Creep of CMSX-4 superalloy single crystals: effects of misorientation and temperature." Acta Materialia **47**(5): 1549-1563.
Matan, N., D. C. Cox, C. M. F. Rae and R. C. Reed (1999). "On the kinetics of rafting in CMSX-4 superalloy single crystals." Acta Materialia **47**(7): 2031-2045.
McGuinty, R. D. (2001). Multiscale representation of polycrystalline inelasticity. Ph.D., Georgia Institute of Technology.
Messerschmidt, U. (2010). Dislocation Dynamics During Plastic Deformation, Springer-Verlag Berlin Heidelberg.
Nabarro, F. R. N. (1996). "Rafting in Superalloys." Metallurgical and Materials Transactions A **27**(3): 513-530.
Nathal, M. V. and R. A. Mackay (1987). "The stability of lamellar γ-γ′ structures." Materials Science and Engineering **85**: 127-138.
Nembach, E. and G. Neite (1985). "Precipitation hardening of superalloys by ordered γ′-particles." Progress in Materials Science **29**(3): 177-319.
Neu, R. W. and D. J. Smith (2011). "Modeling Creep-Fatigue Deformation of Ni-Base Superalloys Using Crystal Viscoplasticity." Journal of ASTM International **8**(5): JAI103674.
Orowan, E. (1940). "Problems of plastic gliding." Proceedings of the Physical Society **52**: 8-22.
Österle, W., D. Bettge, B. Fedelich and H. Klinglehöffer (2000). "Modelling the orientation and direction dependence of the critical resolved shear stress of nickel-base superalloy single crystals." Acta Materialia **48**(3): 689-700.
Ott, M. and H. Mughrabi (1999). "Dependence of the high-temperature low-cycle fatigue behaviour of the monocrystalline nickel-base superalloys CMSX-4 and CMSX-6 on the γ/γ′-morphology." Materials Science and Engineering: A **272**(1): 24-30.
Padture, N. P., M. Gell and E. H. Jordan (2002). "Thermal barrier coatings for gas-turbine engine applications." Science **296**(5566): 280-284.
Perepezko, J. H. (2009). "Materials science. The hotter the engine, the better." Science **326**(5956): 1068-1069.
Pineau, A. and S. D. Antolovich (2009). "High temperature fatigue of nickel-base superalloys – A review with special emphasis on deformation modes and oxidation." Engineering Failure Analysis **16**(8): 2668-2697.

Pollock, T. M. and A. S. Argon (1992). "Creep Resistance of CMSX-3 Nickel-Base Superalloy Single-Crystals." Acta Metallurgica Et Materialia **40**(1): 1-30.
Pyczak, F., B. Devrient and H. Mughrabi (2004). "The effects of different alloying elements on the thermal expansion coefficients, lattice constants and misfit of nickel-based superalloys investigated by X-ray diffraction." Superalloys 2004: 827-836.
Reed, R. C. (2006). Superalloys - Fundamentals and Applications, Cambridge University Press.
Reed, R. C., N. Matan, D. C. Cox, M. A. Rist and C. M. F. Rae (1999). "Creep of CMSX-4 superalloy single crystals: effects of rafting at high temperature." Acta Materialia **47**(12): 3367-3381.
Reed, R. C. and C. M. F. Rae (2014). 22 - Physical Metallurgy of the Nickel-Based Superalloys A2 - Laughlin, David E. Physical Metallurgy (Fifth Edition). K. Hono. Oxford, Elsevier**:** 2215-2290.
Reppich, B. (1982). "Some new aspects concerning particle hardening mechanisms in γ' precipitating Ni-base alloys—I. Theoretical concept." Acta Metallurgica **30**(1): 87-94.
Reppich, B., P. Schepp and G. Wehner (1982). "Some new aspects concerning particle hardening mechanisms in γ' precipitating nickel-base alloys—II. Experiments." Acta Metallurgica **30**(1): 95-104.
Sabol, G. P. and R. Stickler (1969). "Microstructure of Nickel-Based Superalloys." physica status solidi (b) **35**(1): 11-52.
Sarkar, A. and J. K. Chakravartty (2015). "Activation Volume and Density of Mobile Dislocations in Plastically Deforming Zr-1pctSn-1pctNb-0.1pctFe Alloy." Metallurgical and Materials Transactions A **46**(12): 5638-5643.
Sheh, M. Y. and D. C. Stouffer (1988). Anisotropic Constitutive model for Nickel-base Single Crystal Superalloys, NASA Report No. CR-182157.
Shenoy, M., Y. Tjiptowidjojo and D. McDowell (2008). "Microstructure-sensitive modeling of polycrystalline IN 100." International Journal of Plasticity **24**(10): 1694-1730.
Shui, L., S. Tian, T. Jin and Z. Hu (2006). "Influence of pre-compression on microstructure and creep characteristic of a single crystal nickel-base superalloy." Materials Science and Engineering: A **418**(1): 229-235.
Shyam, A. and W. W. Milligan (2004). "Effects of deformation behavior on fatigue fracture surface morphology in a nickel-base superalloy." Acta Materialia **52**(6): 1503-1513.
Srikanth, A. and N. Zabaras (1999). "A computational model for the finite element analysis of thermoplasticity coupled with ductile damage at finite strains." International Journal for Numerical Methods in Engineering **45**(11): 1569-1605.
Sun, Y. Q. and P. M. Hazzledine (1996). "Chapter 49 Geometry of dislocation glide in Ll2γ'-phase: TEM observations." Dislocations in Solids **10**: 27-68.
Tetzlaff, U. and H. Mughrabi (2000). "Enhancement of the High-Temperature Tensile Creep Strength of Monocystalline Nickel-Base Superalloys by Pre-Rafting in Compression
" Superalloys 2000: 173-282.
Tinga, T., W. A. Brekelmans and M. G. D. Geers (2010). "Cube slip and non-Schmid effects in single crystal Ni-base superalloys." Modeling and simulation in material science and engineering **18**.
Vorontsov, V. A., R. E. Voskoboinikov and C. M. F. Rae (2012). "Shearing of γ' precipitates in Ni-base superalloys: a phase field study incorporating the effective γ-surface." Philosophical Magazine **92**(5): 608-634.
Vose, F., M. Becker, A. Fischersworring-Bunk and H. P. Hackenberg (2013). "An approach to life prediction for a nickel-base superalloy under isothermal and thermo-mechanical loading conditions." International Journal of Fatigue **53**: 49-57.
Wahl, J. B. and K. Harris (2012). New Single Crystal Superalloys, CMSX-7 and CMSX-8. Superalloys 2012 Seven Springs Mountain Resort,Seven Springs, PA, TMS.

Wang, A. J., R. S. Kumar, M. M. Shenoy and D. L. McDowell (2006). "Microstructure-based multiscale constitutive modeling of gamma-gamma ' nickel-base superalloys." International Journal for Multiscale Computational Engineering **4**(5-6): 663-692.
Weber, G. R. and S. Ghosh (2016). "Thermo-mechanical deformation evolution in polycrystalline Ni-based superalloys by a hierarchical crystal plasticity model." Materials at High Temperatures **33**(4-5): 401-411.
Wilson, B. C. and G. E. Fuchs (2008). The effect of composition, misfit and heat treatment on the primary creep behavior of single crystal nickel base superalloys PWA 1480 and PWA 1484. Superalloys 2008. K. A. G. R. C. Reed, P. Caron, T. Gabb, M. G. Fahrmann, E. S. Huron, S. A. Woodard. Pennsylvania, USA, The Minerals, Metals & Materials Society.
Yandt, S., X. J. Wu, N. Tsuno and A. Sato (2012). Cyclic Dwell Fatigue Behaviour of Single Crystal Ni-Base Superalloys with/without Rhenium. Superalloys 2012, John Wiley & Sons, Inc.**:** 501-508.
Zamrik, S. Y. and M. L. Renauld (2000). "Thermo-mechanical out-of-phase fatigue life of overlay coated IN-738LC gas turbine material." Thermo-Mechanical Fatigue Behavior of Materials, 3rd Vol **1371**: 119-137.
Zhu, Z., H. Basoalto, N. Warnken and R. C. Reed (2012). "A model for the creep deformation behaviour of nickel-based single crystal superalloys." Acta Materialia **60**(12): 4888-4900.

Table 1. Chemical composition (%w) of superalloys commonly used the hot gas path (Cetel and Duhl 1988, Harris et al. 1992, Reed 2006, Wahl and Harris 2012)

Alloy	Cr	Co	Mo	W	Al	Ti	Ta	Re	Hf	C	B	Zr	Ni
Mar-M247LC-DS	8.4	10.0	0.7	10.0	5.5	1.0	3.0	-	1.5	0.07	0.015	0.05	Bal
CM247LC-DS	8.1	9.2	0.5	9.5	5.6	0.7	3.2	-	1.4	0.07	0.015	0.01	Bal
CMSX-4	6.5	9.0	0.6	6.0	5.6	1.0	6.5	3.0	0.1	-	-	-	Bal
SC16	16.0	0.17	3.0	0.16	3.5	3.5	3.5	-	-	-	-	-	Bal
PWA1484	5.0	10.0	2.0	6.0	5.6	-	8.7	3.0	0.1	-	-	-	Bal
CMSX-8	5.4	10.0	0.6	8.0	5.7	0.7	8.0	1.5	0.2	-	-	-	Bal

Table 2. Physical material parameters

b	2.49 (Å)
F_{attack}	$1x10^{12}$ [1/s]
γ_{APB}	0.111 [J/m^2]
δ	-0.002
T_{melt}	1726 [K]
f_{γ}	*0.3*
$f_{\gamma'}$	*0.7*
L_{γ}	$0.1x10^{-6}$ [m]
$L_{\gamma'}$	$0.8x10^{-6}$ [m]

Table 3. Parameters fitted to creep-fatigue deformation data

c_{annh1}	20.0	n	2.0
c_{annh}^{pbd}	10.0	η_0	20.0
c_{annh2}	5.0	c_{pass11}	3.0
c_{Fdis}	1.0	c_{pass22}	1.5 x10^{-2}
c^{icb}	5.0	c_{pass21}	3 x10^{-3}
c_{jump1}	9x10^{-2}	c_{vc1}	1.0
c_{jump2}	6x10^{-2}	c_{vc2}	8.4x10^{-1}
c_{misfit}	275 [1/mol]	Q_{slip}^{110}	295 [kJ/mol]
c_{mult1}	3x10^{-5}	Q_{slip}^{112}	240 [kJ/mol]
c_{mult}^{pbd}	1x10^{-3}	$\rho_{\gamma}^{(\alpha)}\|_{t=0}$	1x10^{11} [1/m^2]
c_{mult2}	9x10^{-3}	C_{χ}	1x10^{2}
c_{mult21}	5x10^{-15}	κ	1x10^{6}

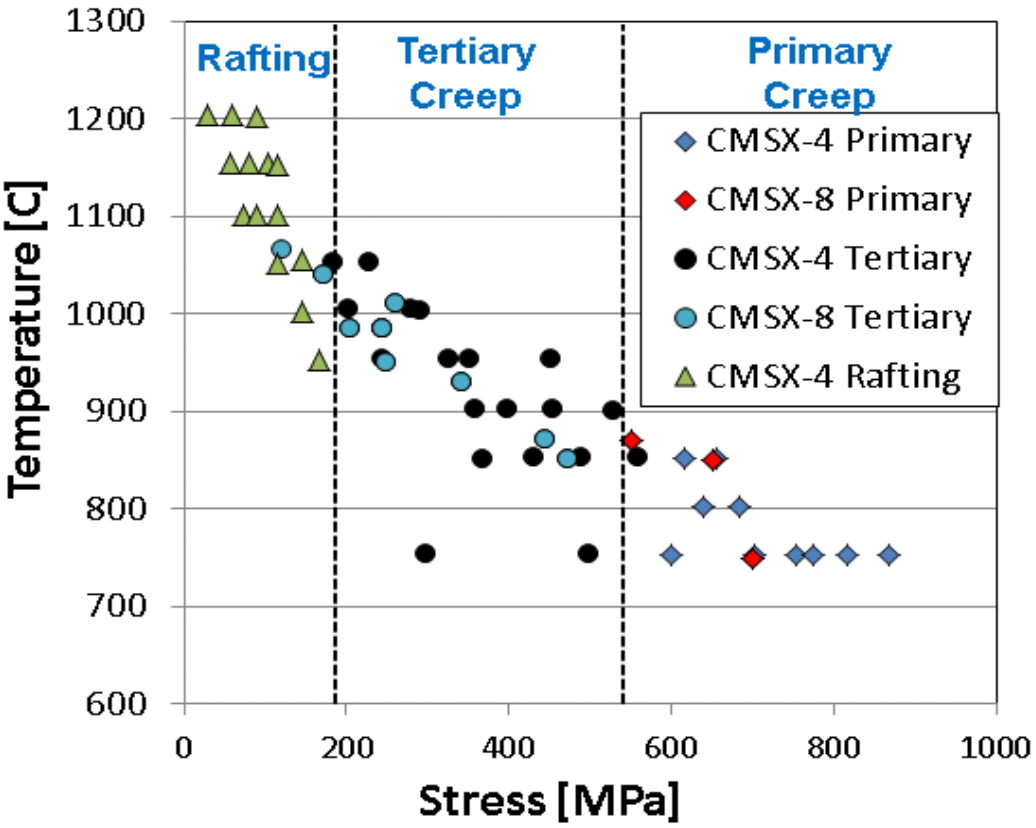

Figure 1: Temperature and stress regimes under which primary, tertiary creep or rafting are the dominant deformation mechanisms, CMSX-4 data taken form reference (Reed 2006)

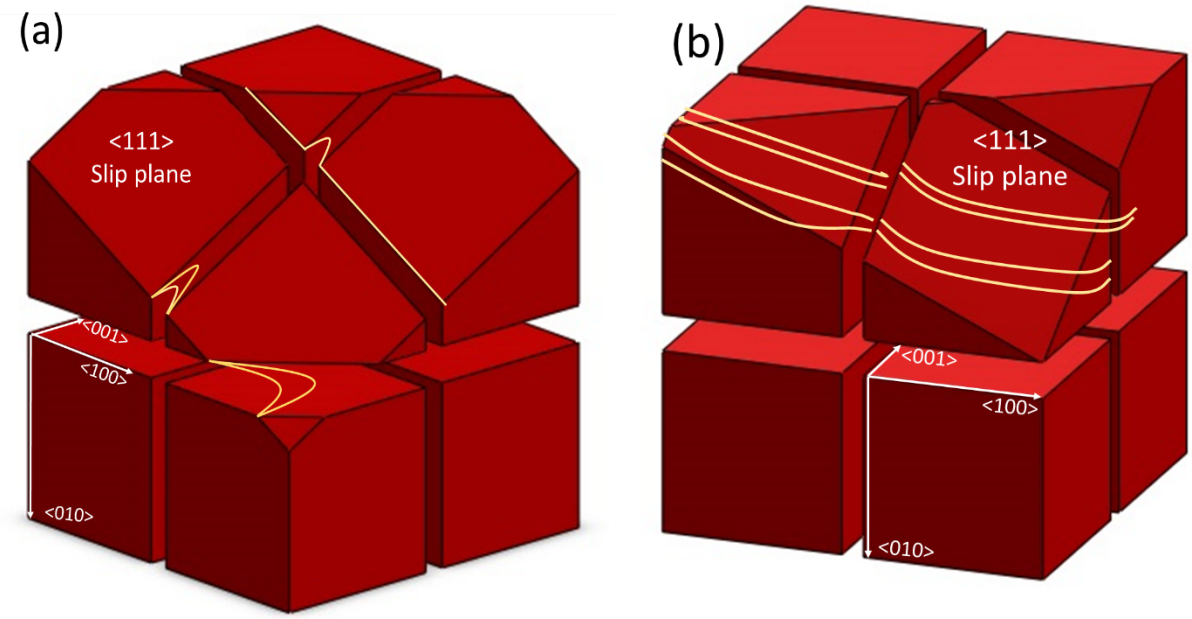

Figure 2. (a) Dislocations of mean spacing $\lambda_{\gamma}^{(\alpha)}$ gliding and climbing in the γ channels in the <111> slip plane (b) Cutting of the γ' precipitates in the <111> slip plane by dislocation of mean spacing $\lambda_{L1_2}^{(\alpha)}$

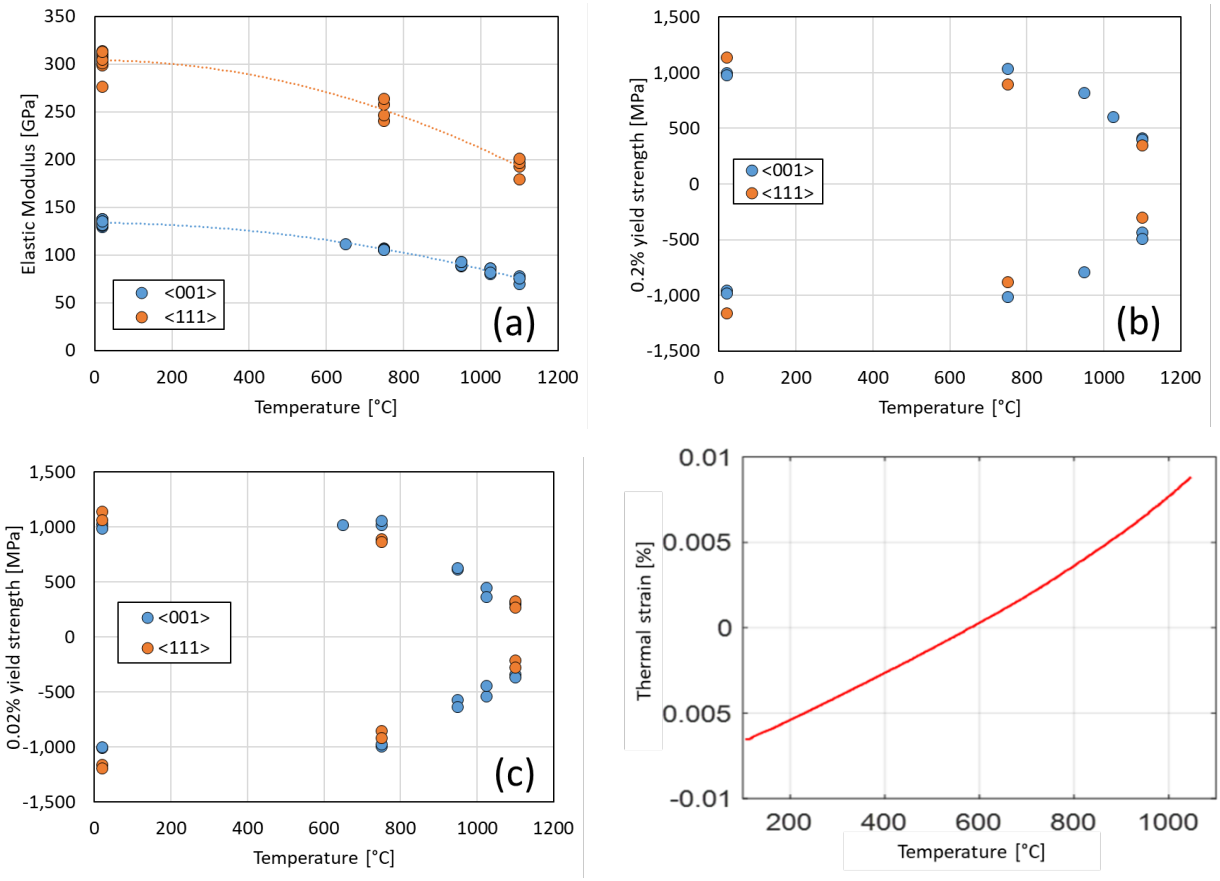

Figure 3: Themoelastic properties of CMSX-8 in the <001> and in the <111> crystallographic orientation: (a) elastic modulus (b) 0.2% yield strength (c) 0.02% yield strength (d) elastic thermal strain

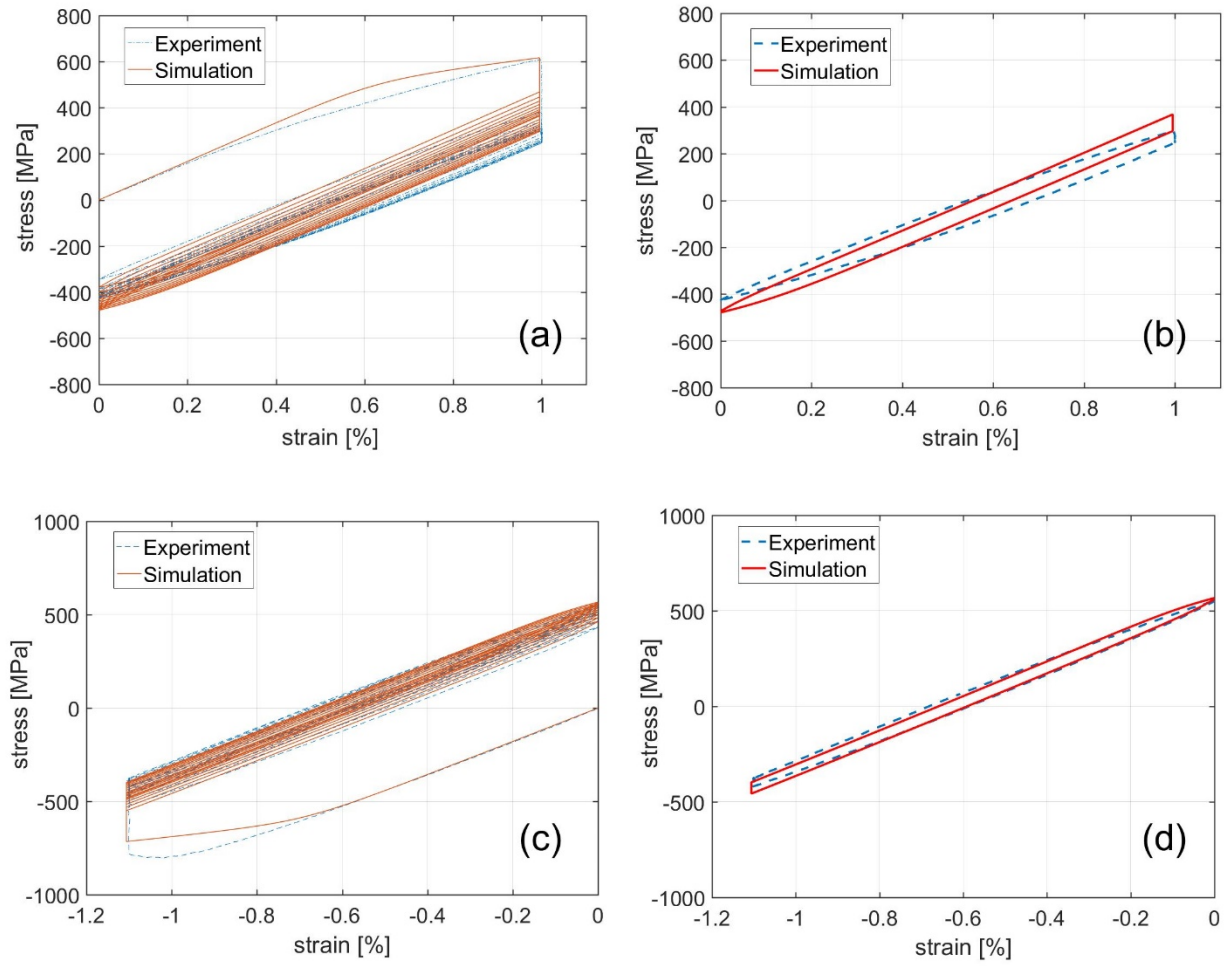

Figure 4. Calibrated model: (a) fist ten cycles (b) stabilized hysteresis of creep-fatigue at 1025°C at strain rate of $1x10^{-3}$ [1/s] with 3 minute holds at maximum tension. (c) first ten cycles (d) stabilized hysteresis of creep-fatigue at 950°C at strain rate of $1x10^{-3}$ [1/s] with 3-minute holds at maximum compression

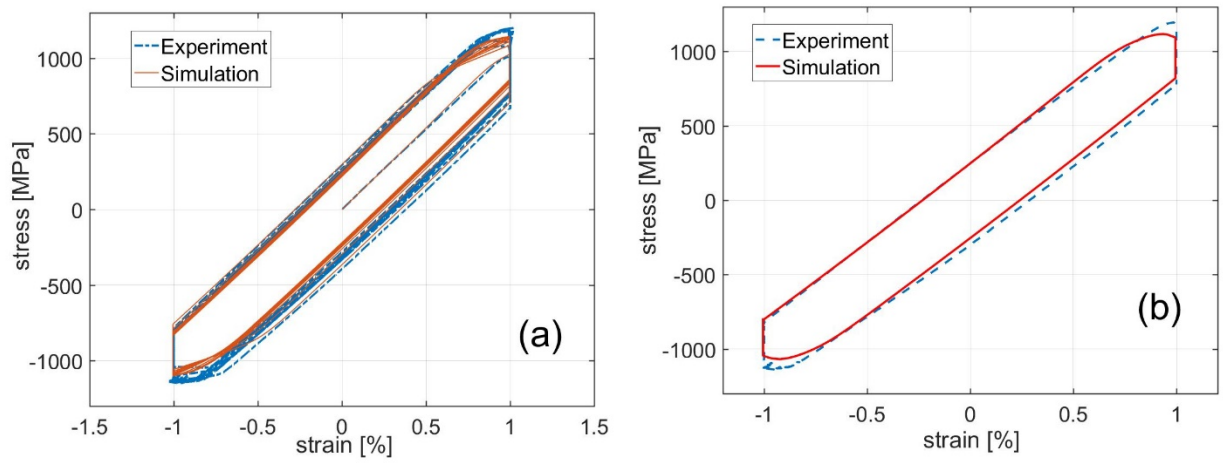

Figure 5. Creep-fatigue model predictions for 750°C at strain rate of $1x10^{-3}$ [1/s] with 20 minute holds at maximum tension and compression: (a) first ten cycles (b) stabilized hysteresis

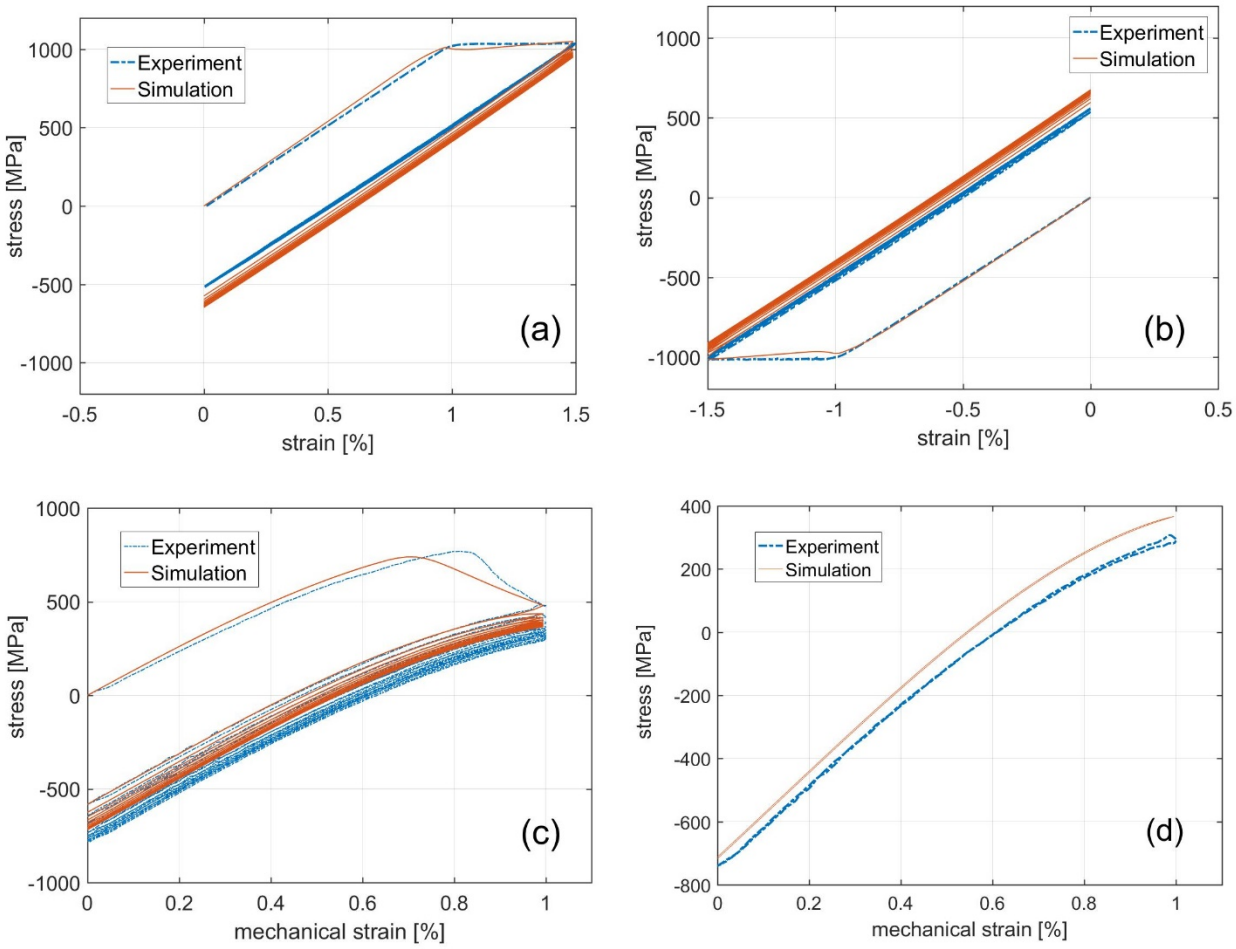

Figure 6: Model validation: (a) and (b) Isothermal fatigue at 750°C with strain rate of $1x10^{-3}$ [1/s]. (c) and (d) Cycles 1 through 10 and stabilized hysteresis respectively of in-phase TMF test from 100°C to 1050°C with heating rate of 2.83 [°K/s]

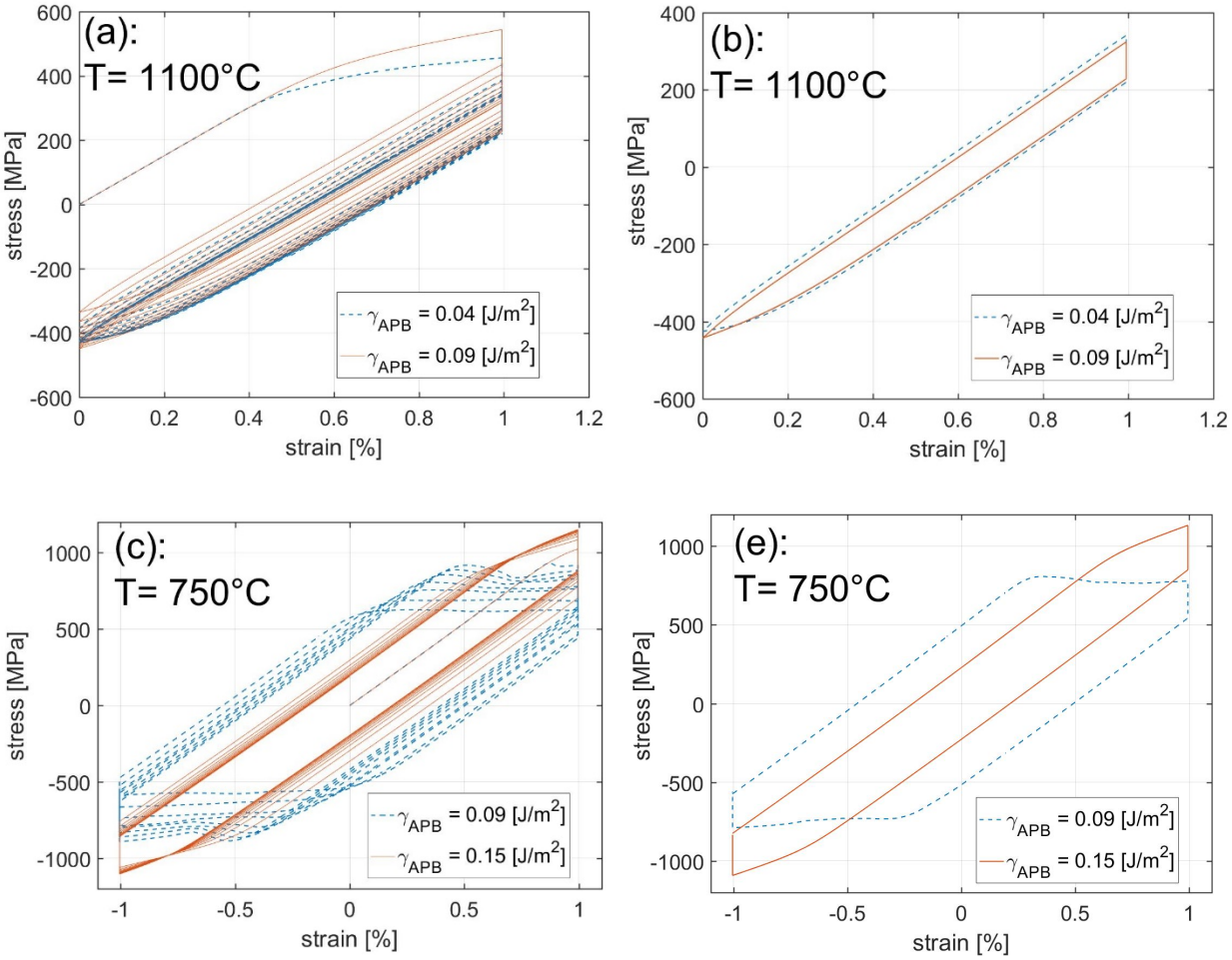

Figure 7. Influence of APBE on mechanical response: (a) first ten cycles (b) stabilized hysteresis of creep-fatigue at 1100°C at strain rate of $1x10^{-3}$ [1/s] with 3-minute holds at maximum tension. (c) first ten cycles (d) stabilized hysteresis of creep-fatigue at 750°C at strain rate of $1x10^{-3}$ [1/s] with 20 minute holds at maximum tension and compression.

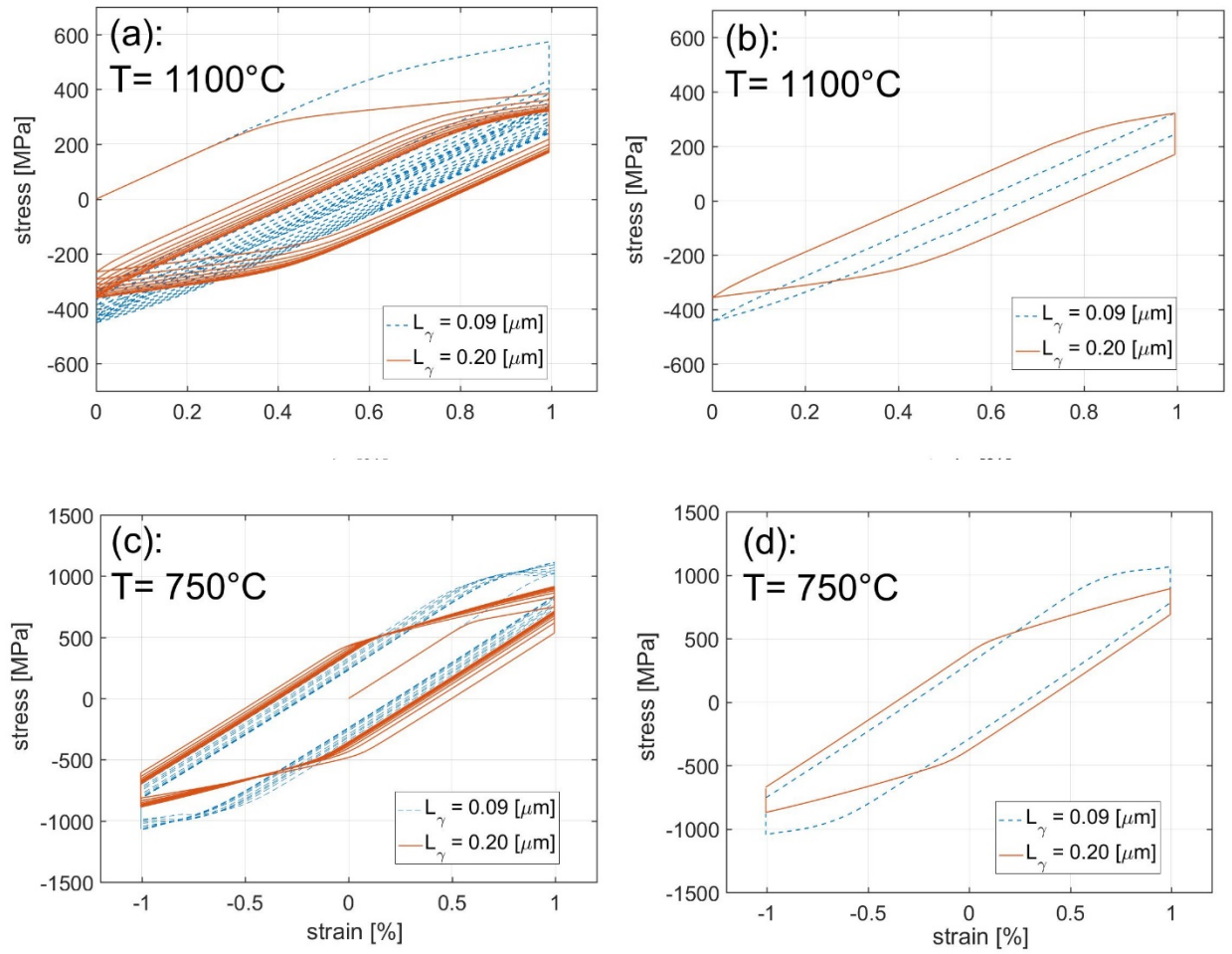

Figure 8. Influence of γ channel size on mechanical response: (a) first ten cycles (b) stabilized hysteresis of creep-fatigue at 1100°C at strain rate of 1x10^{-3} [1/s] with 3-minute holds at maximum tension. (c) first ten cycles (d) stabilized hysteresis of creep-fatigue at 750°C at strain rate of 1x10^{-3} [1/s] with 20-minute holds at maximum tension and compression

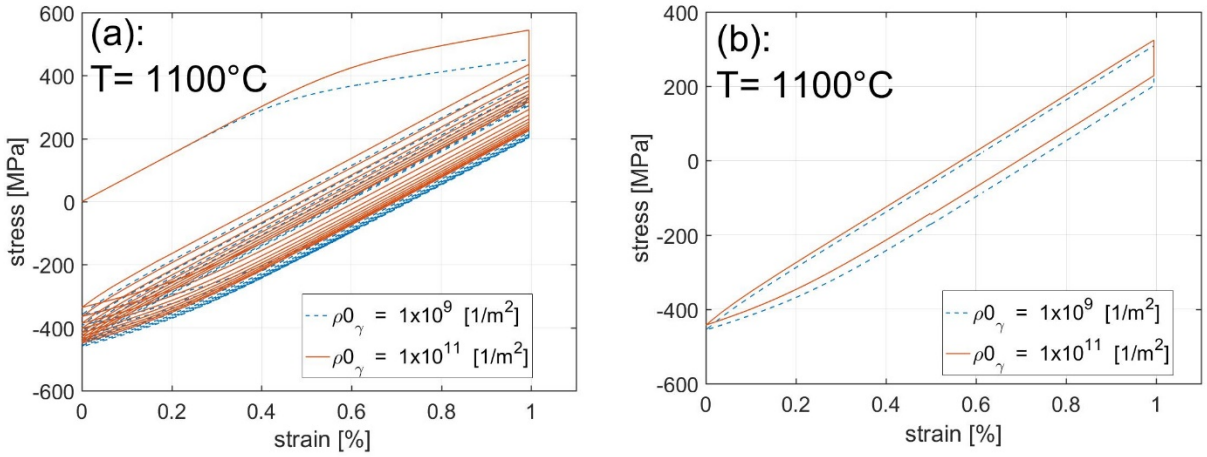

Figure 9: Influence of initial dislocation density in the γ channels on mechanical response: (a) first ten cycles (b) stabilized hysteresis of creep-fatigue at 1100°C at strain rate of $1x10^{-3}$ [1/s] with 3-minute holds at maximum tension.

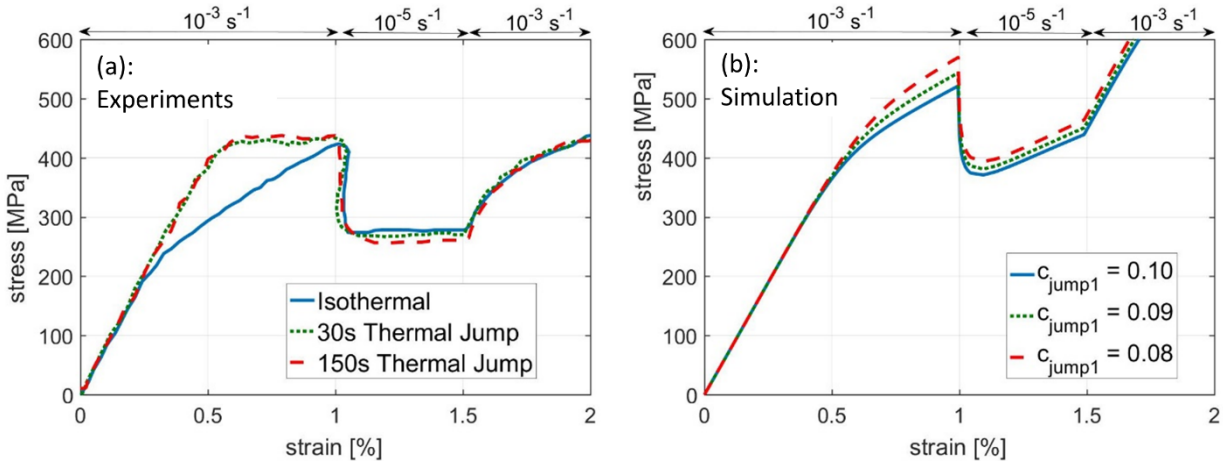

Figure 10. Transient hardening due to temperature jumps: (a) Experimental results on a Single-crystal Superalloy at 1050˚C (le Graverend et al. 2016) (b) Simulation of CMSX-8 at 1100˚C

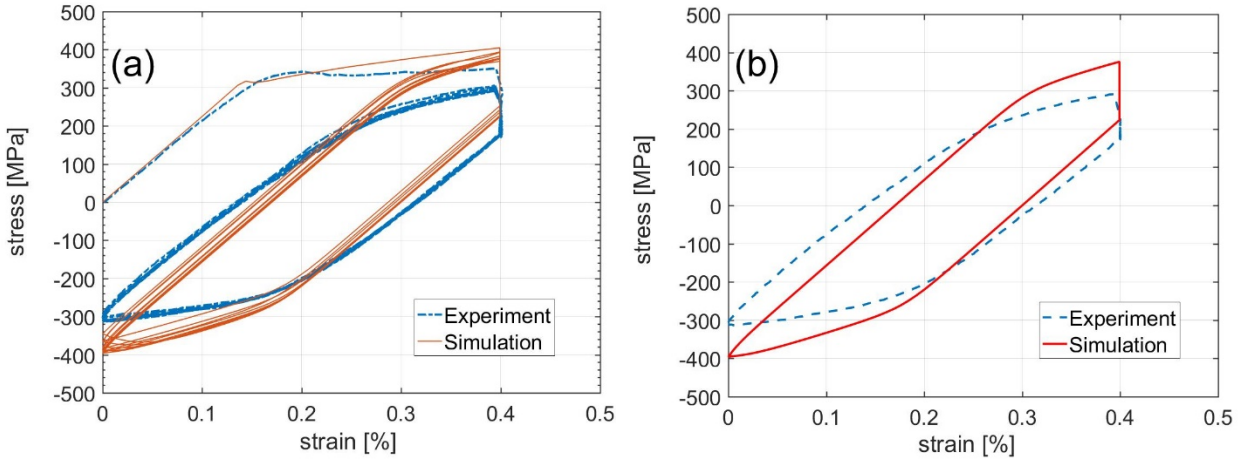

Figure 11: Creep-fatigue at 1100°C at strain rate of 1x10^{-3} [1/s] with 3 minute holds at maximum tension in the <111> crystallographic orientation: (a) first ten cycles (b) stabilized hysteresis

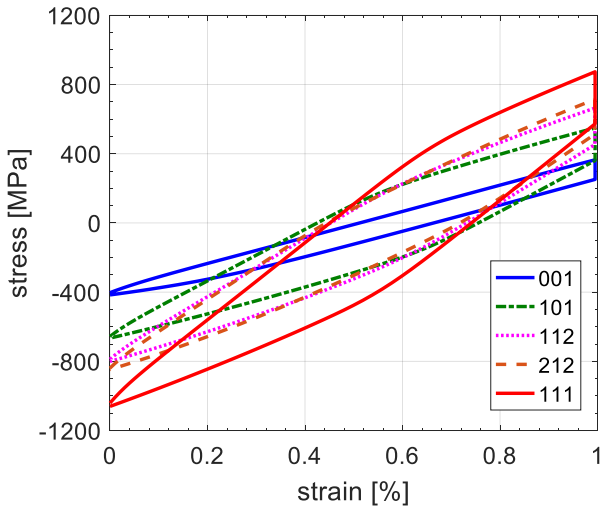

Figure 12: Influence of orientation on strain-controlled constant amplitude response with a 3-minute dwell in tension at 1100°C with strain rate of 1x10-3 [1/s]

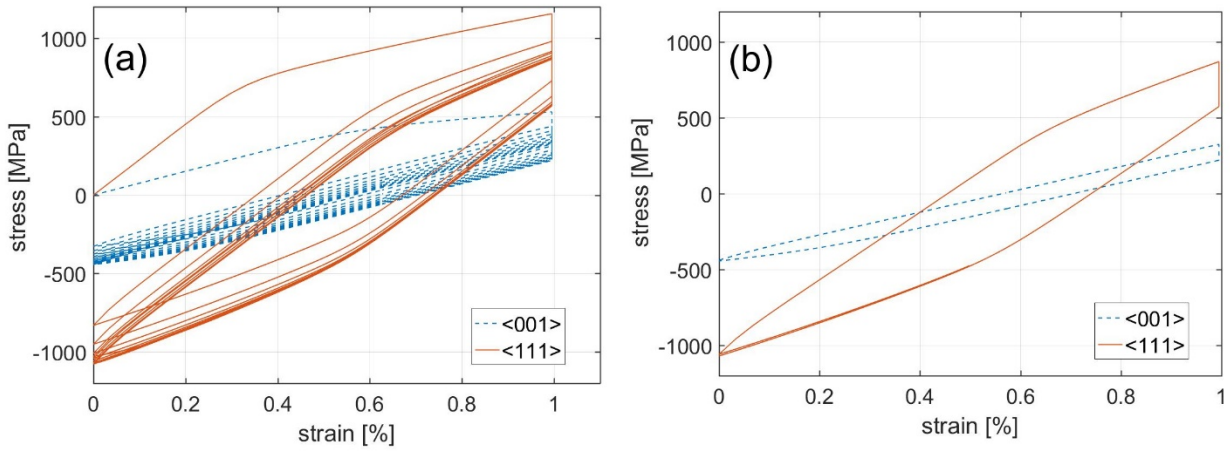

Figure *13*. Simulated creep-fatigue response in the <001> and the <111> orientation at 1100˚C, strain rate of $1x10^{-3}$ [1/s] with 3 minute holds at maximum tension: (a) first ten cycles (b) stabilized hysteresis